Master thesis and internship[BR]- Master's thesis : Uncertainty quantification in the rebuilding free-stream temperature inside the VKI Plasmatron[BR]- Integration internship

Auteur : Chavet, Thomas
Promoteur(s) : Arnst, Maarten
Faculté : Faculté des Sciences appliquées
Diplôme : Master en ingénieur civil en aérospatiale, à finalité spécialisée en "aerospace engineering"
Année académique : 2020-2021
URI/URL : http://hdl.handle.net/2268.2/13288

University of Liège

School of Engineering and Computer Science

Uncertainty quantification in the free-stream temperature measurement inside the VKI Plasmatron

Under the supervision of Prof. **M. Arnst**, **A. Fagnani** and **J. Coheur**

Master's thesis carried out by **Thomas Chavet**
to obtain the degree of Master of Science in **Aerospace Engineering**

Academic year 2020-2021

Abstract

The VKI Plasmatron is a plasma wind tunnel that allow the reproduction of some of the conditions of an atmospheric reentry. A plasma is generated at low subsonic regime at temperatures up to about 10000 K. This temperature is measured by optical emission spectroscopy. More specifically, the procedure focused on the atomic emission of the oxygen and nitrogen lines at 777 nm and 747 nm respectively. In the measurement procedure, many parameters have uncertainties that lead to an error on the temperature computation. In this thesis, the uncertainties on eight parameters are quantified. These uncertainties are then propagated through the measurement chain with the Monte Carlo propagation method. In this case, the propagated uncertainties will depend on the emission line used to retrieve the temperature, so both computations are performed and compared. Each source of uncertainty is also propagated individually to be compared with each other.

Acknowledgements

First of all, I would like to sincerely thank Joffrey Coheur and Andrea Fagnani for their help throughout my work on this thesis. Thank you for your explanations, your precious advice and your confidence. I appreciated working on this project and I thank you for it.

I would also like to thank Prof. M. Arnst who allowed me to work on this subject and who guided me in the preparation of this work.

Finally, I am deeply grateful to my family and my friends for their help and their numerous advice. I also thank you for your moral support during this pandemic.

Contents

Chapter 1

Introduction

The atmospheric reentry is a critical part of a space mission. During this phase, the spacecraft enters the Earth's atmosphere at a speed of 8 km/s. The spacecraft should slow down to a sufficiently low speed to open its parachute. This enormous amount of kinetic energy is converted into heat during the reentry (see Fig 1.1). That heat is a real threat for the spacecraft as it could result in its disintegration and even in the death of astronauts in the case of a manned mission. To avoid that, thermal protection systems are used in order to absorb the heat and evacuate it by radiation or by ablation of the shield. Some spacecrafts however do not need to come back to earth and once they reach the end of their life span they reenter the atmosphere to prevent an overpopulation of space debris in space. The heat from reentry is used to disintegrate these spacecraft so that they are not a threat for the population on the ground.

FIGURE 1.1: Atmospheric reentry of NASA Orion spacecraft

1.1 Plasma wind tunnels

The design of spacecrafts intended to reenter the atmosphere requires a very good understanding of the physical reactions and constrains applied on it during reentry. After 60 years of space exploration, a lot of data have been collected during atmospheric reentry such as temperatures, pressures, mechanical loads, etc. However, after the design of a component, its behaviour during reentry should still be tested. As a test in real condition is extremely expensive, a solution has been developed to perform on ground testing at lower costs. This solution consists of plasma wind tunnels that can reproduce part of the conditions of an atmospheric reentry [10]. In the facility, thermal

protection materials can be placed downstream of the plasma jet to simulate a reentry.

There are different types of plasma wind tunnels. In the past, more attention has been paid to arc and induction plasma wind tunnels. This type of facility makes it possible to carry out tests on a large scale and at high enthalpy [2]. However, the flow in these arc-jet facilities is polluted by the erosion of the electrodes and the electrode particles in the flow have an impact on the chemical reaction on the thermal protection material.

Induction type facilities are another type of plasma wind tunnel that have much better flow purity and can be used for the study of aerothermochemistry and gas–surface interaction phenomena [15]. The Plasmatron (Fig 1.2) at the von Karman Institute (VKI) is one of these facilities. With a power of 1200 kW, it is the most powerful induction-coupled plasma wind tunnel in the world. Inside the Plasmatron chamber, a plasma can be generated at temperatures up to about 10000 K and at a pressure between 5 and 200 mbar[1]. The speed of the jet is low subsonic ($Ma \approx 0.1$) and measured by a water-cooled pitot tube. This low speed implies that the pressure is almost constant in the chamber. Local thermodynamic equilibrium can be assumed in the chamber because the flow has a low velocity and the pressure is sufficiently high [8]. The plasma is air heated with inductively coupled plasma (ICP) torch. The torch generates an oscillating magnetic field from a radio frequency current. By Faraday's law, this magnetic field induces an oscillating electric field in the torch. In the plasma, the free electrons are accelerated by this electric field and their temperature increases. The other particles will finally increase their temperature by colliding with the high energy electrons.
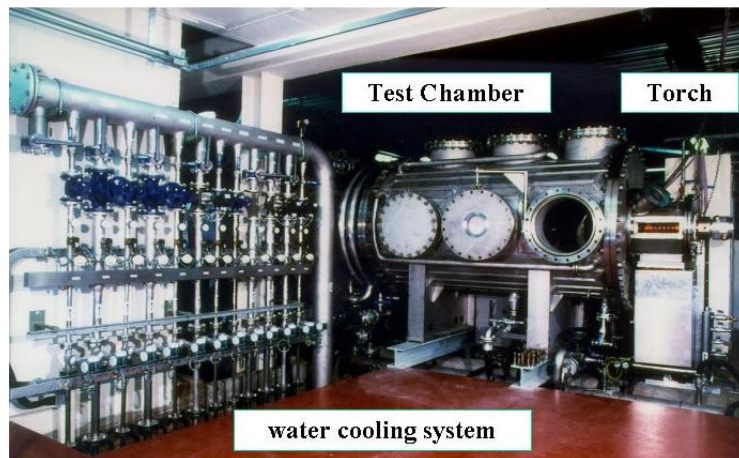
FIGURE 1.2: Plasmatron facility at VKI.

The Plasmatron is used to study the reaction of a material exposed to the conditions of an atmospheric reentry. Different plasma flow properties can be used in order to simulate reentries in different atmospheres [16]. A precise characterization of the flow is necessary to accurately define the test conditions. The method used in this thesis to measure the thermodynamic properties of the flow is optical emission spectroscopy [12]. It offers the advantage of being non-intrusive and remains simple to perform with respect to other methods such as laser induced fluorescence. This

---

[1]https://www.vki.ac.be/index.php/research-consulting-mainmenu-107/facilities-other-menu-148/plasma-facilities/71-1200-kw-induction-plasmatron

technique has been used to measure the temperature inside the Plasmatron for several operating conditions by Fagnani et al. [7]. Several spectrum measurements were performed to increase the accuracy of the results.

1.2   Optical emission spectroscopy

Optical emission spectroscopy consists in measuring the spectrum of the light emitted by a body. Due to the temperature, the atoms and molecules constituting the body will emit photons at different wavelengths depending on the species. The emitted light is spectrally dispersed in order to measure the energy emitted in each wavelength. This technique can be used to determine the chemical composition of a body. By measuring the intensity emitted in some wavelengths and if the temperature is known, it is even possible to determine the concentrations of the components. In this case, optical emission spectroscopy is used to retrieve the temperature of the plasma [3]. It can be done because the components of the plasma are known and their concentrations can be deduced assuming local thermodynamic equilibrium.

Optical emission spectroscopy has the advantage of measuring the parameters of the plasma without interacting with it. Unfortunately, this method also has the main drawback that the detected radiation is integrated over the line of sight. This means that the emitted light passes through the plasma and might be reabsorbed or scattered. However, this phenomenon is very small in this case and will be neglected for simplification. The fact of having a plasma almost transparent implies that the background light is also measured. Finally, the temperature is computed from the local emission but only the radiation integrated over the line of sight is measured as it can be seen in Fig 1.3. An Abel inversion is applied to the measurement to retrieve the local emission. This Abel inversion is a mathematical development that relates the local values to the integrated values.
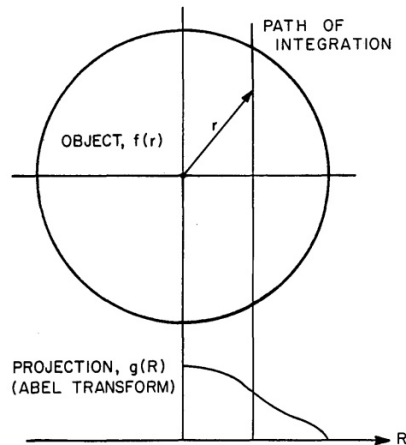
FIGURE 1.3: Schematic of the local emissions that are integrated over a line of sight to result in the measured radiance [9].

At very high temperatures, the atoms and molecules present in the plasma radiate their energy by means of three mechanisms [7]. The first mechanism is continuous radiation, which means that it can radiate in all wavelengths within a certain range. It happens when free electrons are deflected by the electric field produced by the ions

(free-free transitions). The second mechanism is also continuous radiation and is produced when the free electrons recombine with ions (bound-free transitions). The third mechanism is discrete radiation, which means that it can only emit energy in certain wavelengths. It is produced when atoms and molecules transit from a high energy state to a lower energy state (bound-bound transitions). This transition produces a photon that has the same energy as the difference of energy between the two states. This implies that one type of transition will always produce photons of the same wavelength.

In practice, the light emitted by the plasma is focused by mirrors and spectrally resolved by a grating. The spectrum is finally measured by a camera. The image should be processed in order to recover the emission of the plasma. This processing includes cleaning the signal from background noise, calibration and Abel inversion. The details of each of these steps are explained in chapter 2. Once the emission of the plasma has been computed, the temperature can be recovered in different ways.

A first method uses simulations of plasma emissions. From databases of atom transitions, a simulation of the spectrum emitted by the plasma can be performed. This simulation takes as input the temperature, the pressure and the chemical composition of the plasma. By assuming LTE and fixing the pressure, a spectrum can be fitted to the measurement to retrieve the temperature. However, this method requires a very accurate simulation of the spectrum and can therefore be very demanding in computations. For example, the code SPECAIR used at VKI for the temperature computation is simulating 37 molecular transitions and radiation lines of N, O and C atoms [13].

A second method, which is the one used in this thesis, is based on the discrete radiation of atoms transiting between two states of known energy. The photons emitted by one type of transition all have exactly the same wavelength. Therefore, they can be isolated from the other radiations by spectral dispersion and the total energy emitted by this type of transition can be measured. This quantity of energy depends on the temperature and the density of atoms. Since the pressure and the molar fractions are known, the temperature can be computed from this measurement. This technique is faster to compute than the fitting method because only one emission line is considered here while the whole spectrum is used for the fitting method, which will make the propagation of uncertainties a lot less demanding in computation time.

1.3   Objectives and overview

After measuring the temperature of the plasma inside the Plasmatron an uncertainty analysis is required in order to be confident on these results. For this thesis, a code for the temperature computation from spectroscopic measurements has been implemented along with an uncertainty analysis. The first objective of this thesis is to determine the source of uncertainty in the temperature measurement. For each uncertain parameter, the uncertainties should be quantified as well as their probability distribution (uniform, Gaussian, etc). The second objective is to propagate those uncertainties through the measurement chain and to evaluate their impact on the final measure of the temperature.

One similar uncertainty quantification has been performed by Laux [14] for a different ICP facility. That analysis accounted for the uncertainty on three main parameters: the uncertainty on the measurements, on the absolute calibration and on the Einstein

coefficient. The propagation of these uncertainties has been done by analytical developments. In this thesis, the same three uncertainty sources are taken into account but in order to increase the accuracy of the results, five additional sources of uncertainty are considered. Furthermore, the propagation method differs since a numerical method is adopted for this thesis. The use of a numerical method is much easier to implement than an analytical method because it does not depend on the measurement procedure and the code can be used as a black box. However, it has the drawback of requiring a lot of computations. Nevertheless, an analytical propagation inspired by Laux has been performed in this thesis in order to be compared with the results of the numerical method.

This work is divided in five main parts, the first being this introduction. In the second chapter, the procedure of the temperature measurement is described. Every step is explained with an example of a temperature computation from a real spectrum measurement taken at the Plasmatron. The third chapter is dedicated to the theory of uncertainty quantification. The characterization of uncertain parameters is explained as well as the Monte Carlo method used to propagate those uncertainties. In the fourth chapter, each step is recomputed by taking the uncertainties into account. The sources of uncertainties are first identified and measured. Afterwards, the uncertainties on the parameter are propagated using the Monte Carlo propagation method. Then, in the last section of the same chapter, the uncertainties on the temperature measurement are computed considering all uncertain parameters combined. The different sources of uncertainties considered in this analysis are also summarized and compared. Finally, some conclusions are drawn in the last chapter with recommendations for further work.

Chapter 2

Measurement procedure

The details of the temperature measurement by optical emission spectroscopy are described in this chapter. The process is detailed at each step with an example of a temperature computation from a real spectrum measurement taken at the Plasmatron. In this chapter, the computation is performed without taking any uncertainties into account.

The measurement of the temperature can be divided in a few simple steps that are computed one after the other. This chain can be summarized in a flowchart with inputs, computation boxes and outputs as displayed in Fig 2.1. Here, the uncertain inputs are represented with blue boxes and the computation boxes are in red. Only parameters with uncertainties are displayed. All the measurement steps are explained in the following sections.

Spectrum image of plasma

Spectrum image of calibration source

Background noise

Background subtraction

Background subtraction

Radiance of calibration source

Calibration

Baseline subtraction

Line selection and integration

Spatial dimension

Abel inversion

Einstein coefficient (A_u)

$\epsilon_{\text{ul}} = \frac{E_{\text{u}} - E_1}{4\pi} \mathcal{A}_{\text{ul}} n_{\text{u},i}$

Pressure

$n_{\text{u},i} = n_i \left(T_{\text{LTE}}, p\right) \frac{g_{\text{u},i} \exp\left(-\frac{E_{\text{u},i}}{k_{\text{B}} T_{\text{LTE}}}\right)}{Q_{\text{int},i}(T_{\text{LTE}})}$
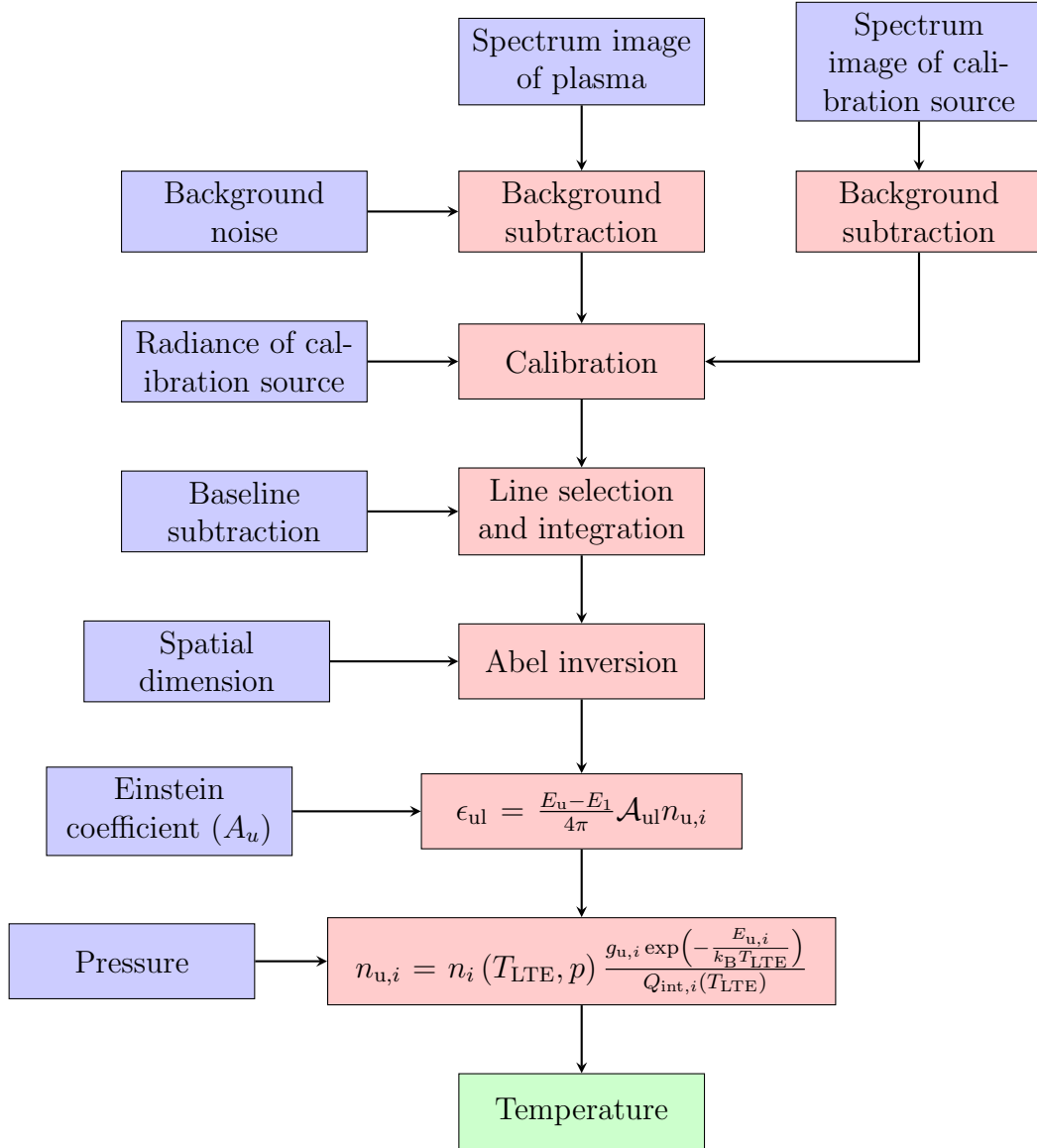
Temperature

FIGURE 2.1: Flowchart summarizing the chain of the temperature measurement of the plasma inside the Plasmatron with the blue boxes as uncertainty inputs and the red boxes as computation boxes.

2.1 Measurement of the spectrum

The first step consists in measuring the light emitted by the plasma and only one slice of the jet is measured at a time. A slit is used for the slice selection and can be shifted along the jet direction to measure a different slice. Then, mirrors and a diffraction grating are used to resolve and focus the spectrum on a CCD camera as depicted in Fig 2.2. The detector is a PI-MAX3 from Princeton Instruments that has a size of 1024 by 1024 pixels and a pixel size of 12.8 µm.
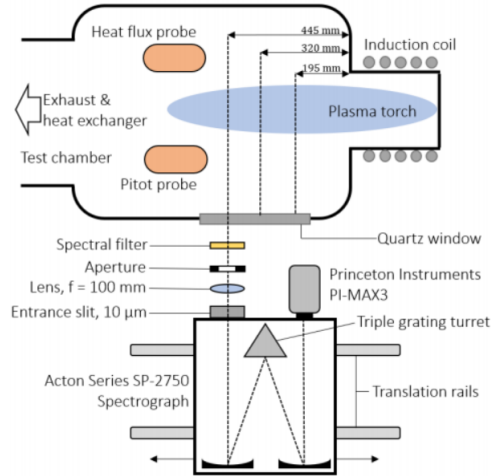

FIGURE 2.2: Schematic of the experimental set-up, showing the Plasmatron chamber and the components of the spectral imaging system [7].

An example of an image taken by the camera is depicted in Fig 2.3. The horizontal axis corresponds to the wavelength of the photons, measured in a range of 100 nm. The vertical axis is the spatial dimension of the jet. The camera is placed in order to have the jet at the center of the detector. The camera measures the photons emitted by the atoms and molecules constituting the plasma. These components emit photons following the three mechanisms explained above.
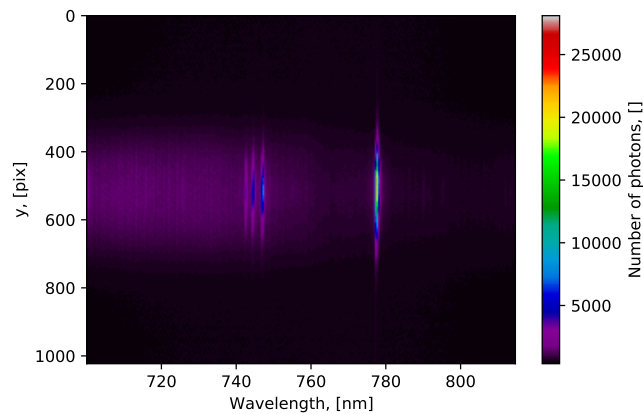

FIGURE 2.3: Example of a raw spectrum image taken by the camera.

The signal measured by the camera is disturbed by a background noise. This noise is due to some reflections of the light by the walls but also to the infrared emission of the camera or the walls. The signal is then a combination of the plasma emission and

this background noise. The noise can induce a small bias in the final determination of the temperature, it is therefore subtracted from the spectrum measurement. The noise is measured by taking a spectrum image of the Plasmatron chamber under the same conditions, without the plasma. This background spectrum is then subtracted from the raw image to obtain a spectrum accounting only for the photons emitted by the plasma.

2.2   Calibration

The image obtained after the first step is a 2D matrix where each pixel takes a numerical value that characterizes the intensity of the radiation. However, this value depends on the parameters of the camera such as the exposure time or the gain that amplifies the signal. Thus, a calibration must be performed in order to retrieve the value of the radiance of the plasma which is defined as the energy emitted by the plasma and received by a given surface, expressed in $W/(m^2\ nm\ sr)$. In order to perform the calibration, the plasma is replaced by a tungsten lamp of a known radiance. The same configuration and conditions are used to take a spectral image of the lamp. The radiance of the plasma is then retrieved from the formula:

$$L_\lambda^{\mathrm{meas}} = \frac{S^{\mathrm{meas}}/\Delta t^{\mathrm{meas}}}{S^{\mathrm{calib}}/\Delta t^{\mathrm{calib}}} L_\lambda^{\mathrm{calib}}, \tag{2.1}$$

where $L_\lambda^{\mathrm{meas}}$ is the unknown radiance of the plasma and $L_\lambda^{\mathrm{calib}}$ is the radiance of the tungsten lamp in $W/(m^2\ nm\ sr)$. These two radiances are both a function of the wavelength. S^{meas} and S^{calib} are the intensities measured at each pixel, for the plasma and the tungsten lamp, respectively, after the background subtraction. Finally, Δt^{meas} and $\Delta t^{\mathrm{calib}}$ are the exposure times of the camera. These two times are different because the tungsten lamp is much more radiative than the plasma and $\Delta t^{\mathrm{calib}}$ must be shorter to avoid saturation of any pixels of the camera. As the calibration depends on the wavelength and the signals, this calibration equation is applied on each pixel individually.

2.3   Line selection and integration

The calibrated measurements are a function of the wavelength and the radial coordinate. However, only a small portion is useful for the next steps. Indeed, the atoms in the plasma that transit between two states emit light in a very particular wavelength and only the measurement of one type of transition is required for the computation of the temperature.

The first step is to choose the atom transition and therefore the corresponding emission line. Here the best choice would be the atomic transition that corresponds to the strongest emission line. This line has the higher signal to noise ratio and will therefore provide a better precision. In order to better see the strength of the different lines, the central line of Fig 2.3 is plotted in Fig 2.4. In this figure, four emission lines can be clearly identified. The three small peaks at 742.4, 744.2 and 746.8 nm correspond to the emission of nitrogen atoms transiting from a high energy electronic configuration to a lower energetic level. The larger peak at 777 nm is in fact the sum of three different transitions of oxygen atoms emitting in a very close wavelength range (777.2, 777.4 and 777.6 nm) which is called a triplet.

Any peak can be used for the temperature computation. Here, this larger peak is chosen because it has the highest signal to noise ratio. Since the peak is the combination of three very close emission line, the total radiance of the peak is the sum of the radiance of the three emission line. A comparison of the temperatures computed from the peak at 777 nm and the peak at 747 nm is done in section 4.6 in order to study the effect of a lower signal to noise ratio on the temperature and the uncertainty.
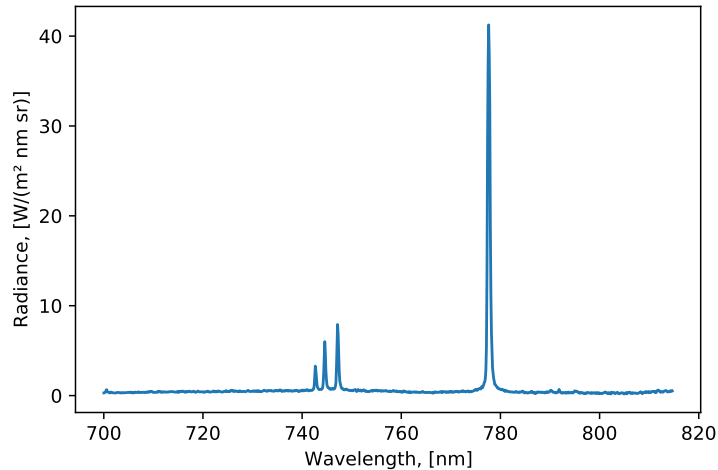

FIGURE 2.4: Radiance of the center of the plasma jet as a function of the wavelength showing four strong emission lines.

In Fig 2.4, it can also be seen that, even if the atoms emit in one given wavelength, the camera does not measure a perfectly sharp peak. The peak is a bit broadened, mainly due to the grating and other optical instruments that are not perfect. Because of this broadening, the radiance must be integrated over a small range of wavelengths in order to retrieve the total radiance of the emission line.

Unfortunately, the plasma is composed of many atoms and molecules and some of them emit photons at the exact same wavelength as the peak. This peak is actually the sum of the emission line and some other small continuous radiations emitted by molecules. The intensity of the emission line is almost ten times greater than the intensity of the molecules radiation. It is unfortunately impossible to isolate the radiation of the emission line from the other molecules radiation. The only way to measure the radiance of the emission line is to estimate these small molecule radiations and subtract it to the total radiance of the peak. Away from the peak, the radiance measured is only due to these molecules radiation. Knowing this, the molecules radiation is approximated by a line that fits the radiations on both sides of the peak. The line is fitted to the points that are far enough from the peak so that these points are not influenced by the emission line.

Concretely, the computation is performed as follows: two integration points are chosen on both sides of the peak. Then, the peak is integrated between these two bounds in order to retrieve the total radiance. Finally, a line is drawn between the two integration points and the area below this line (corresponding to the approximation of the base radiations) is subtracted from the total radiance. Fig 2.5 shows the integration of the peak of the oxygen emission triplet (three emission lines) with the radiance that is due to the oxygen radiation (in blue) and the approximation of the molecule radiations that is called the baseline (in red).
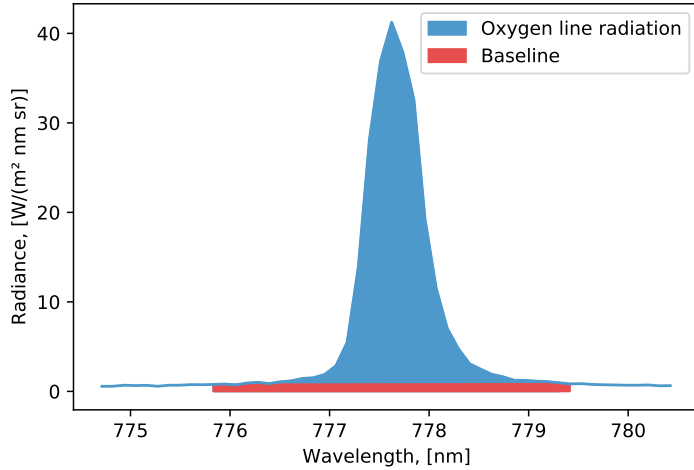
FIGURE 2.5: Zoom in Fig 2.4 centered at 777 nm showing the emission intensity of the oxygen triplet and the baseline emission.

This graph is plotting the radiance for one radial coordinate (the center of the jet) but the integration should be performed for all radial coordinates. The result of the integration and the baseline subtraction is then a scalar which is a function of the spatial coordinate corresponding to the radiance of oxygen atoms for the three types of transition. This radiance is plotted in Fig 2.6 for all radial coordinates.

In Fig 2.6, a spatial calibration has been performed to convert the spatial coordinate, that has a size of 1024 pixels to mm. It has been measured that this image of 1024 pixels long corresponds to a length of 200 mm. After finding the center of the plasma which is fixed at 0 mm, the radial coordinate r is computed for each pixel.
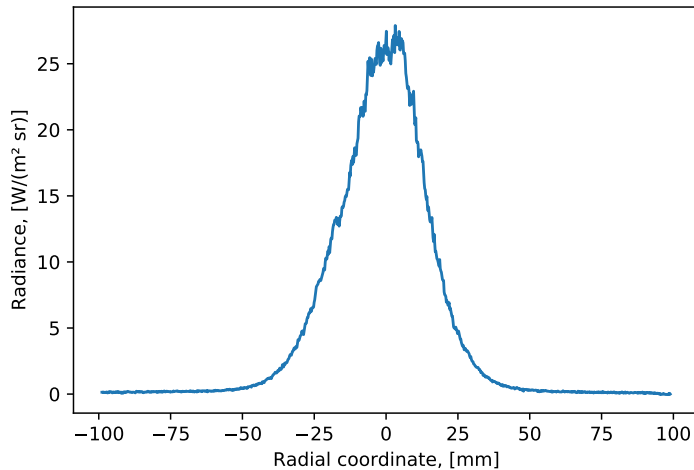

FIGURE 2.6: Spatial emission of oxygen triplet (Integrated between 776 nm and 779 nm).

A careful attention should be paid to the distinction between Fig 2.5 and Fig 2.6. Indeed, both functions have a similar shape but have a completely different interpretation. Fig 2.5 is the emission of the oxygen triplet as a function of the wavelength for one radial coordinate (here the center line). For each radial coordinate, the baseline and the blue area are computed and Fig 2.6 plot the size of the blue area for each coordinate. After a certain coordinate ($r = \pm 50$ mm), the signal measured is mainly due to the baseline radiation and the emission of the oxygen triplet is close to 0.

2.4 Abel inversion

The light is emitted by the whole volume of the jet which means that the radiance measured by the camera is the sum of the local emissions on a line of sight.
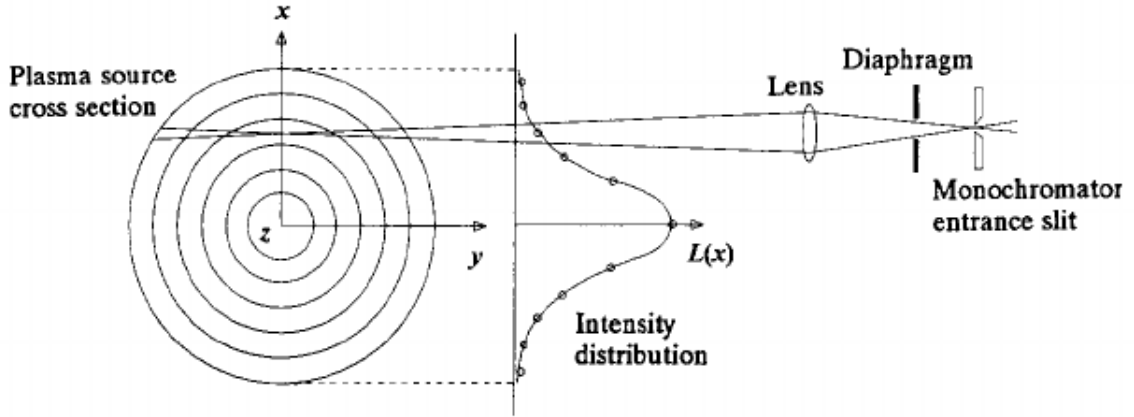

FIGURE 2.7: Diagrammatic representation of Abel inversion geometry for observations of plasma sources with cylindrical cross section. [17]

If the plasma is optically thin and radially symmetric, meaning that it does not absorb the light it emits, then the radiance measured by the camera is simply the integration of the local emission and can be computed with the equation:

$$L_\lambda(y) = 2 \int_y^R \frac{\epsilon_\lambda(r)r}{\sqrt{r^2 - y^2}} dr, \tag{2.2}$$

where $L_\lambda(y)$ is the radiance measured on a line of sight, $\epsilon(r)$ is the local emission depending only on the radius from the center of the jet and R is the edge of the jet where the emission is assumed to be null.

In this case, the radiance is known since it has been computed in the previous step and the local emission is needed for the temperature computation. Equation 2.2 should then be reversed to express the local emission as a function of the radiance leading to the Abel inversion equation:

$$\epsilon_\lambda(r) = -\frac{1}{\pi} \int_r^R \frac{dL_\lambda(y)}{dy} \frac{dy}{\sqrt{y^2 - r^2}}. \tag{2.3}$$

Unfortunately, this equation cannot be applied directly because the derivative of the radiance $L_\lambda(y)$ must be computed and this term is very sensitive to noise. The curve must first be smoothed to account only for the global variation of the curve that is the variation that is due to the temperature. An example of the radiance and the smoothing is given in Fig 2.8.

In this figure, it can also be seen that the radiance is not perfectly symmetrical. Indeed, due to buoyancy, the top half of the plasma is a little hotter (the right part of the graph) than the bottom part (the left of the graph). This problem is solved by taking the average of the top and the bottom part. It is mandatory that the smoothed curve is symmetrical because the Abel inversion can only be applied on a radially symmetrical profile.
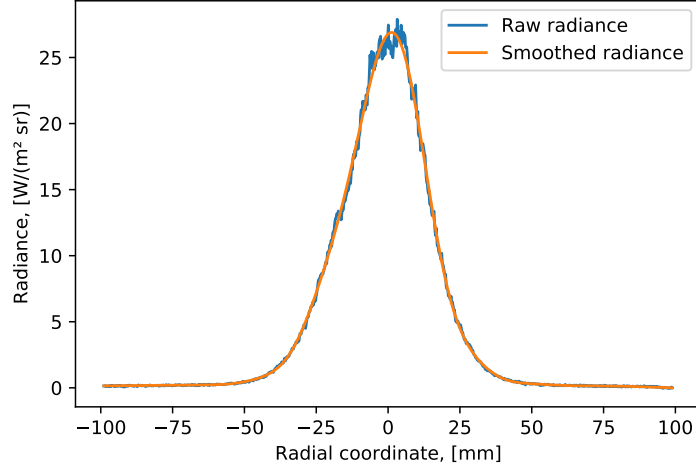
FIGURE 2.8: Example of the noisy radiance computed in Fig 2.6 and a smoothing of the curve.

Now, the Abel inversion equation (Eq. 2.3) is applied to the smoothed curve to give the local emission which is radially symmetric and thus depends only on the distance to the center. By symmetry, only one half of the curve is inverted and plotted in Fig 2.9.
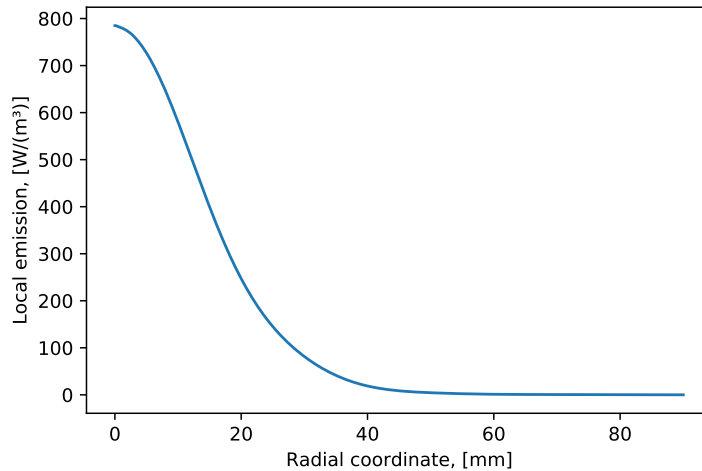

FIGURE 2.9: Local emission of oxygen triplet (776 nm - 779 nm).

To recapitulate, Fig 2.8 represents the radiance of the plasma (in $W/(m^2 \ sr)$) which is the energy received by the camera. Fig 2.9 on the other hand, represents the local emission of the plasma (in W/m^3) which is the energy radiated by the atoms in all directions by one unit of volume.

2.5 Temperature computation

An atom in an exited level emits light when changing its state to a less energetic level. The intensity of this emission is computed from Eq. 2.4 [12].

$$\epsilon_{\mathrm{u}} = \frac{E_{\mathrm{u}} - E_{1}}{4\pi} \mathcal{A}_{\mathrm{u}} n_{\mathrm{u},i} \tag{2.4}$$

16

Where ϵ_{u} is the local emission computed in the previous step. E_{u} and E_{l} are the energy of the two states retrieved from the NIST database[1] which provides these values with great accuracy (on the order of a few percent). The Einstein coefficient $\mathcal{A}_{\mathrm{u}}$ is the number of atoms that transit between the two states per second.

From this equation the population of the atoms $n_{\mathrm{u},i}$ is firstly computed. Secondly, if this population follows a Boltzmann distribution then it can be computed with Eq. 2.5. The Boltzmann distribution is only valid for plasma in local thermodynamic equilibrium (LTE), that is achieved when the different species constituting the plasma (atoms, molecules, electrons, etc) all have the same temperature. In this case, the ICP torch transmits energy only to the electrons and LTE is therefore not reached in the heating zone. However, at 100 mbar, the pressure is sufficiently high so that the electrons rapidly transmit their energy to the other particles and LTE can be assumed in the chamber. This assumption can lead to uncertainties but they are very difficult to estimate. Moreover, since the plasma is very close to LTE, these uncertainties are probably small and for these two reasons, they will not be considered in this thesis.

LTE is then assumed meaning that the population $n_{\mathrm{u},i}$ follows a Boltzmann distribution that is computed with:

$$n_{\mathrm{u},i} = n_i\left(T_{\mathrm{LTE}}, p\right) \frac{g_{\mathrm{u},i} \exp\left(-\frac{E_{\mathrm{u},i}}{k_{\mathrm{B}} T_{\mathrm{LTE}}}\right)}{Q_{\mathrm{int},i}\left(T_{\mathrm{LTE}}\right)}. \tag{2.5}$$

$g_{\mathrm{u},i}$ and k_{B} are the degeneracy of the energy level and the Boltzmann's constant, respectively. Both are constant given in the NIST database. $Q_{\mathrm{int},i}$ is the internal partition function and is a function of the temperature only. The ground population n_i is the density of the atoms in the least energised level and depends on the temperature and the pressure. This population is computed with Mutation++, a library developed at VKI [18].

The temperature is finally computed with Eq. 2.5 by subtracting $n_{u,i}$ from both sides and using a root-finding algorithm. The method used is the Newton-Raphson method where the slope at each iteration is computed by resolving Eq. 2.5 for T and T+1 K. The temperature is computed for different radial coordinates in order to retrieve the curve of the temperatures as a function of the radius of the jet as depicted in Fig 2.10. In this figure, the temperatures computed from the oxygen triplet 777 nm is plotted along with the temperatures computed from the nitrogen line 747 nm in order to compare the temperatures computed from different lines.

---

[1]National Institute of Standards and Technology. This database contains critically evaluated NIST data for radiative transitions and energy levels of atoms and atomic ions. [11]
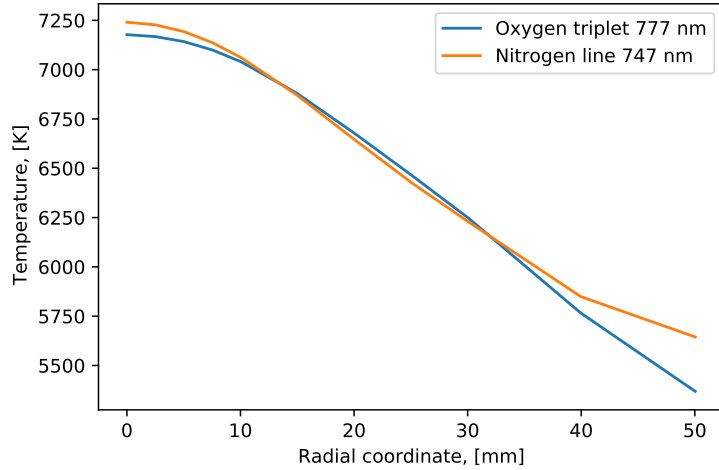
FIGURE 2.10: Temperatures of the plasma computed from the three emission lines of oxygen between 776 nm and 779 nm and from the nitrogen line of 747 nm.

2.6 Validation of the code

The code used to compute the temperature from a spectrum image should now be validated. On that purpose, an external program called SPECAIR [13] is used to simulate a spectrum from a given temperature. Afterwards, the temperature computed from this synthetic spectrum is compared with the temperature given in input to SPECAIR. The other inputs are the pressure and the mole fractions of molecules and atoms. SPECAIR is capable of computing chemical reactions and the final mole fraction of components at a given temperature but only for a pressure close to 1 atm. For this reason, the validation is performed at a pressure of 1 bar and the final mole fractions are computed automatically from an initial mixture of 78.8% of nitrogen, 21.18% of oxygen and 0.02% of carbon which correspond to the mixture of the air in the Plasmatron. The validation is performed for five temperatures: 7300 K, 7000 K, 6500 K, 6000 K and 5000 K. The results are compiled in Fig 2.11 in comparison with the five input temperatures.

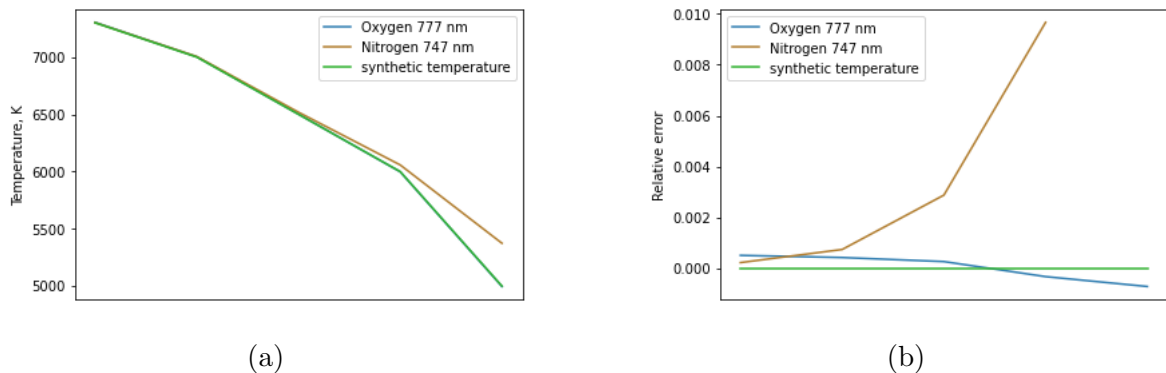(a)   (b)

FIGURE 2.11: Computation of the temperatures from a synthetic spectrum generated with SPECAIR.

The validation shows that the code is very good at retrieving the temperatures from the oxygen triplet 777 nm. However, for the temperatures computed from the nitrogen

18

line 747 nm, the errors are larger at lower temperatures. The spectrum generated by SPECAIR does not need to be calibrated and has no noise. The only approximation in the temperature computation is the baseline subtraction. The errors on this validation can therefore be explained by this baseline subtraction. The errors are larger on the temperatures computed from the nitrogen line because this line radiates less energy than the oxygen and therefore the signal to baseline ratio is lower. This effect is even more pronounced for lower temperatures where the radiation of nitrogen is of the same order of magnitude as the base radiations.

In order to prove that these errors are due to the signal to baseline ratio and the baseline subtraction, SPECAIR is used to compute the energy radiated by the oxygen and the nitrogen atoms only and ignoring the baseline radiation. Computing the temperatures from these clean signals leads to Fig 2.12, where the recovered temperatures now have relative errors lower than half a percent.
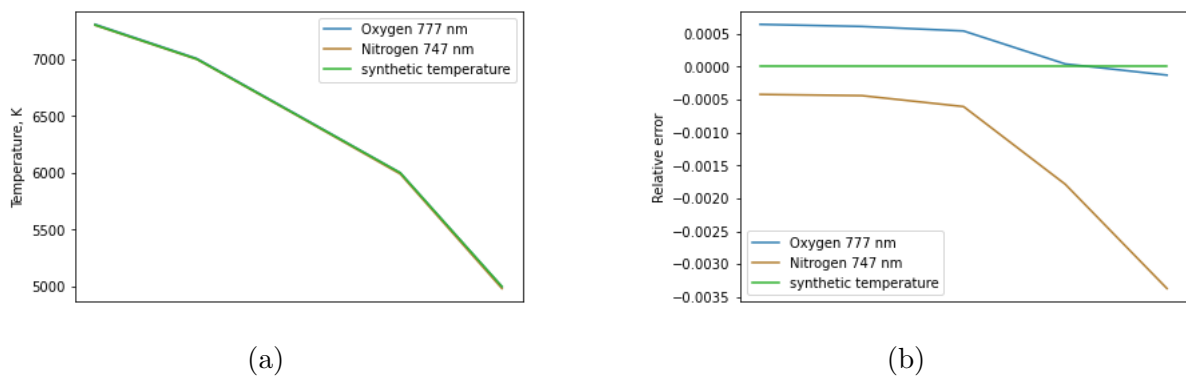

(a)   (b)

FIGURE 2.12: Computation of the temperatures from a synthetic spectrum generated with SPECAIR without the baseline radiation.

Chapter 3

Theory of uncertainty quantification

3.1   Modeling of the measurement chain

The program computing the temperature from a spectrum measurement can be resumed as the function:

$$T(r) = f(x_1, ..., x_m, r), \tag{3.1}$$

where the variables x_i are the inputs to the measurement chain and $T(r)$ is the computed temperature depending on the radial coordinate. In the temperature measurement, many parameters have uncertainties that lead to an uncertainty in the final temperature. The first step is to characterize the uncertainties on the inputs. Then, in a second step, these uncertainties are propagated through the measurement chain using the Monte Carlo method [6, 19].

3.2   Characterization of uncertainties on inputs

In this analysis, eight uncertainties (the eight blue boxes in Fig 2.1) are considered and propagated to the temperature computation. Of course, more than eight parameters have uncertainties and are involved in the temperature computation but only these eight could have been investigated due to time constrain. However, they are the main parameters involved in the computation and the other parameters have either small uncertainties or a small impact on the temperature. The propagation of these uncertainties is done by the Monte Carlo method. It consists in considering all parameters with uncertainties as random variables:

$$\mathbf{X} = (X_1, ..., X_m), \tag{3.2}$$

where X_i is a random variable characterizing a parameter. For each random variable corresponds a probability distribution function P_{X_i}. This function characterizes, for any given subset $\mathcal{A}$ of $\mathbb{R}^m$, the probability $P_{X_i}(\mathcal{A})$ for the random variable X_i to be equal to this subset $\mathcal{A}$.

For example, the pressure inside the Plasmatron has been measured at 100 mbar with an uncertainty of 2%. Unfortunately, this uncertainty alone is not a probability distribution function and assumptions should be made. Many solutions are possible

but two reasonable choices would be either to consider that the uncertainty of 2% is a strict bound and that the probability distribution function is constant between these two bounds as depicted in Fig 3.1. Another solution could be to say that the probability distribution function is a normal distribution and that the 2% of uncertainty is a confidence interval corresponding to two times the standard deviation as plotted in Fig 3.2. This confidence interval has a probability of 95% of containing the real pressure.
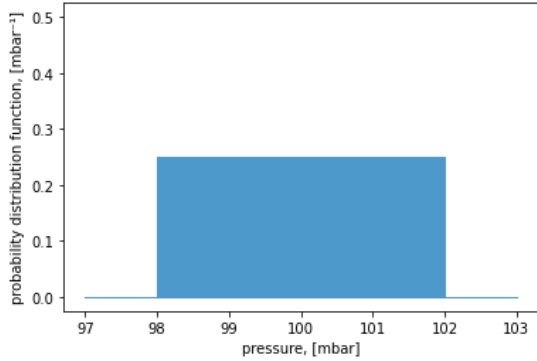
FIGURE 3.1: Probability distribution function of the random variable characterizing the pressure assuming a uniform distribution.
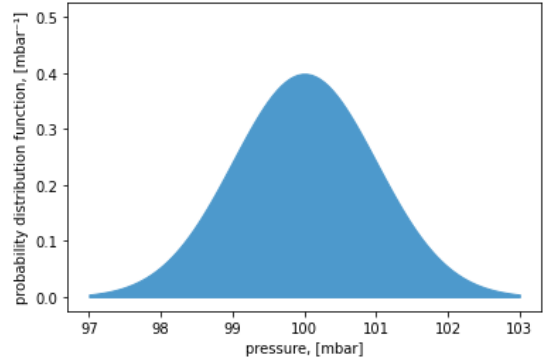
FIGURE 3.2: Probability distribution function of the random variable characterizing the pressure assuming a normal distribution.

3.3 The Monte Carlo propagation method

Considering the temperature computation at one radial coordinate, the measurement chain can be expressed as a function of the inputs:

$$Y = f(X_1, ..., X_m), \tag{3.3}$$

with Y that is the random variable characterizing the temperature. The objective of this thesis is to determine the probability distribution function P_Y of this random variable. Probability theory states that [1]:

$$P_Y(\mathcal{A}) = P_{\mathbf{X}}(\mathcal{B}) \qquad \mathcal{B} = \{\mathbf{X} \in \mathbb{R}^m : f(\mathbf{X}) \in \mathcal{A}\} \tag{3.4}$$

The probability that the temperature is included in a subset $\mathcal{A}$ is equal to the probability that the inputs are contained in a subset $\mathcal{B}$ such that any points in $\mathcal{B}$ results in a temperature included in $\mathcal{A}$. In other words, if a set of inputs has a probability P_1 of being observed, then the temperature computed from those inputs also has a probability P_1 of being observed.

This statement means that taking a random realisation of the set of inputs $\mathbf{X}$ and computing the temperature from these inputs is the same as taking a random realization of the temperature from its probability distribution function. Performing this process a large number of time will lead to many random realizations of the temperature that can be used to compute an estimation of the probability distribution function of the random variable characterizing the temperature.

The Monte Carlo propagation method is a very simple way to perform uncertainty propagation. It has the advantage to be nonintrusive, which means that the code computing the temperature can be used as a black box since only the inputs vary and no modifications of the code are required. One drawback of this method is that it requires a lot of computations. Fortunately, the computation of the measurement chain takes a fraction of a second and, therefore, thousands of samples can be computed in a few minutes.

Chapter 4

Uncertainty propagation through the measurement chain

In the following sections, the temperature is recomputed by taking the uncertainties into account where each uncertain input is analyzed independently. First, the source of uncertainty is discussed and the probability distribution function of the input is determined. Afterwards, one thousand iterations of the measurement chain are performed by taking a random realization of this input for each iteration while all other parameters remain constant. The one thousand temperatures computed at the center of the jet are then compiled in a histogram plot. Finally, a normal distribution function is fitted to this histogram and the standard deviation σ of this normal distribution is computed. For each computation, a confidence interval is provided. This interval corresponds to the mean temperature plus or minus two times the standard deviation ($T_{mean} \pm 2\sigma$). By the definition of the normal distribution, this interval has a probability of 95% of containing the real temperature. In section 4.6, the uncertainty propagation is applied considering the uncertainty on all parameters combined.

4.1 Measurement of the spectrum

4.1.1 Error due to unsteadiness

A first bias comes from the fact that the plasma is not steady [5]. The plasma is oscillating with an unknown amplitude at a high frequency. The frequency of the oscillation is faster than the time of capture of the camera [4]. This means that the signal measured by the camera is an integration of the intensity of the light emitted by the plasma over many oscillations. The emission of a plasma as a function of its temperature follows an exponential shape (Eq 2.4 and Eq 2.5). Therefore, the temperature computed from the average radiance is not the average of the temperature. Since the camera can only measure the average radiance, this results in a bias in the measurement of the temperature. In order to measure this bias, a simulation is performed considering an oscillating temperature of amplitude A. Then, the oscillating emission is computed and averaged. Finally, the temperature is retrieved from this mean emission and plotted in Fig 4.1 for several amplitude of temperature oscillation.
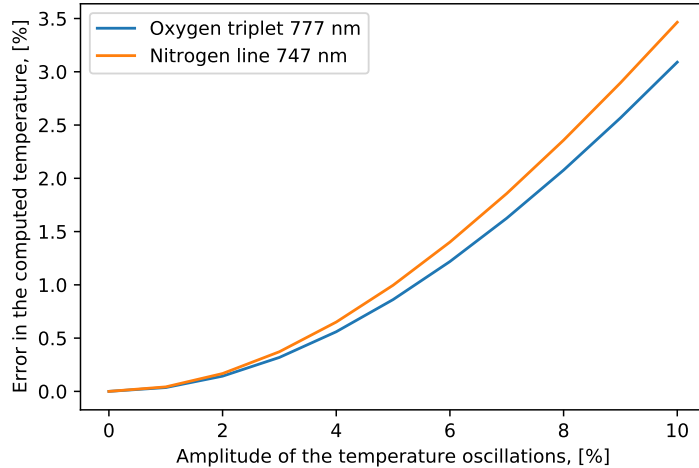
FIGURE 4.1: Error in the temperature computed from an oscillating light emission.

This graph plots the error on the temperature computed from the average light emission with respect to the average temperature. The error computed is always positive which leads to the conclusion that taking an average of the radiance always leads to an overestimation of the temperature of a few percent. This bias is not an uncertainty. Indeed, if the amplitude of the oscillation is known, the bias can be removed by reducing the temperature by the corresponding error. Unfortunately, since the amplitude of the oscillation is hard to estimate so this bias will not be considered on the measurement chain.

4.1.2 Uncertainty on the spectrum image

The CCD camera takes an image of the spectrum emitted by the plasma. It is however very difficult to characterize the uncertainties of these images. this can be due to the fact that the camera is not perfect or that some pixels might be dead or saturated. In addition, some photons can be absorbed or reflected away by the air, the grating or even the plasma itself. A very simple method used to quantify these uncertainties is to take more images. In this way, as each image is subjected to the uncertainties, they are samples of a random variable and for a sufficiently large number of realizations, it is possible to draw the probability distribution function of this variable. Here, ten images of the spectrum are provided and are used to estimate the uncertainties.

Now, these ten images could be used directly in the measurement chain by randomly taking one of the ten images at each iteration but using always only the same ten images is not very representative of the reality. One better way is to generate these images from a normal distribution. First, the mean and the variance of each pixel are computed. Then, the intensities of the pixels are randomly generated considering a Gaussian distribution with the computed mean and variance. A drawback in this case is that the images are 1024 by 1024 pixels which means that more than one million values must be generated. Furthermore, the covariance of each pixel with the other pixels should be computed in order to have accurate random generations. This covariance matrix would be a one million by one million matrix which is simply impossible to compute. To solve this problem, only two cases of correlation are considered: either each pixel is independent and the covariance matrix is diagonal or on the contrary the pixels are fully correlated and the covariance matrix is filled with ones except the

diagonal. These two cases have the advantage of being easy to compute and of being the most extreme cases. Therefore, comparing the two will give a good idea of the influence of the correlation between the pixels on the final uncertainty on the temperature. An example of an image randomly generated considering uncorrelated pixels is shown in Fig 4.2 next to an image randomly generated considering fully correlated pixels in Fig 4.3.
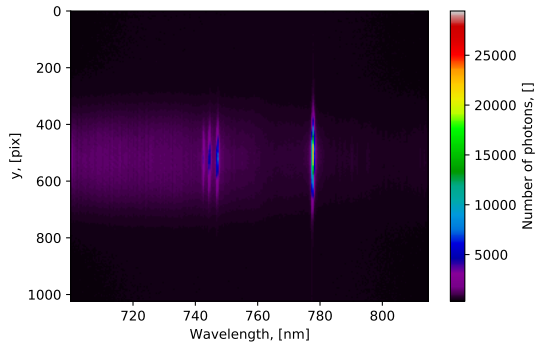

FIGURE 4.2: Image randomly generated from the mean and the standard deviation of the pixels (uncorrelated).
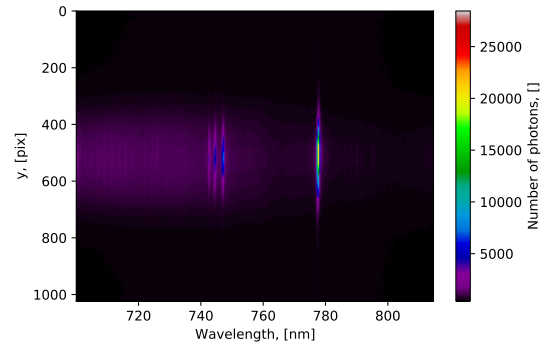
FIGURE 4.3: Image randomly generated from the mean and the standard deviation of the pixels (fully correlated).

These two images appear to be very similar but in fact they can result in very different temperature determinations. In order to have a better appreciation of the variations in these images, the temperature is first computed from each of the ten sample images and depicted in Fig 4.4. Then, one thousand images considering uncorrelated pixels are generated and the temperatures at the center of the plasma jet computed from each of the images are compiled in a histogram plot in Fig 4.5. The same procedure is performed considering fully correlated pixels in Fig 4.6.
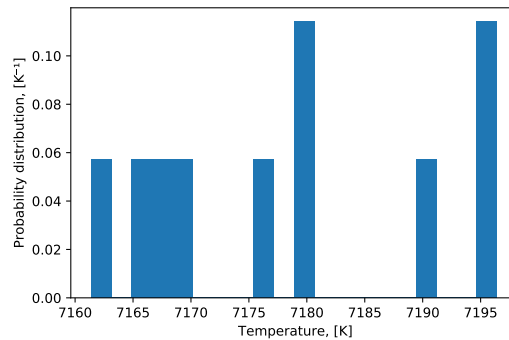
FIGURE 4.4: Temperature computations from each of the 10 measurement images.
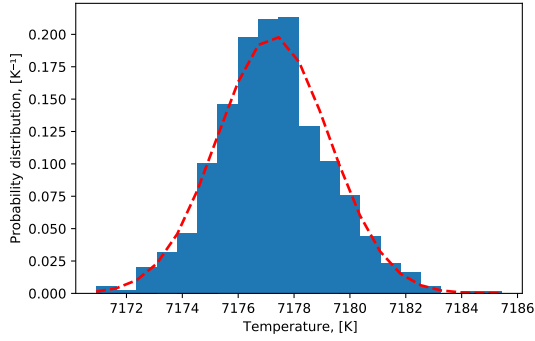
FIGURE 4.5: Temperature at the center of the jet considering the uncertainty on the spectrum image for the uncorrelated case.
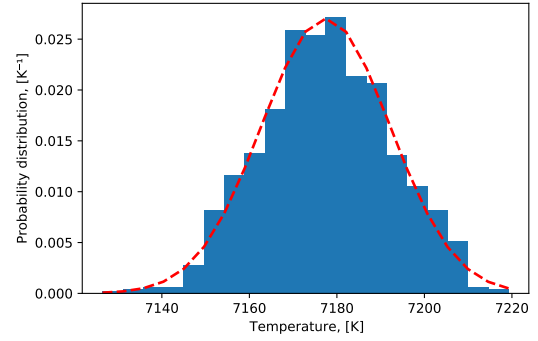

FIGURE 4.6: Temperature at the center of the jet considering the uncertainty on the spectrum image for the fully correlated case.

The ten measurement images yield temperatures in the interval 7180±15 K. For the uncorrelated case, the normal distribution fitted has a standard deviation of 1.95 K meaning that 95% of the temperatures are contained in the interval 7177±3.9 K. On the other hand, for the fully correlated case, the normal distribution has a standard deviation of 14.75 K meaning that 95% of the temperatures are contained in the interval 7177±30.5 K. Since the ten measurement images yield temperatures in a range between these to cases, it can be concluded that the pixels of the spectrum image have some correlations. The random process that generates the spectrum image is somewhere between these two extreme cases. In the end, only fully correlated pixel images are considered since it is the case with the largest range. In this way, the actual uncertainties are guaranteed to be within the computed range.

The maximum error corresponding to two times the standard deviation is computed for each radial coordinate and plotted in Fig 4.7.

(a)

(b)
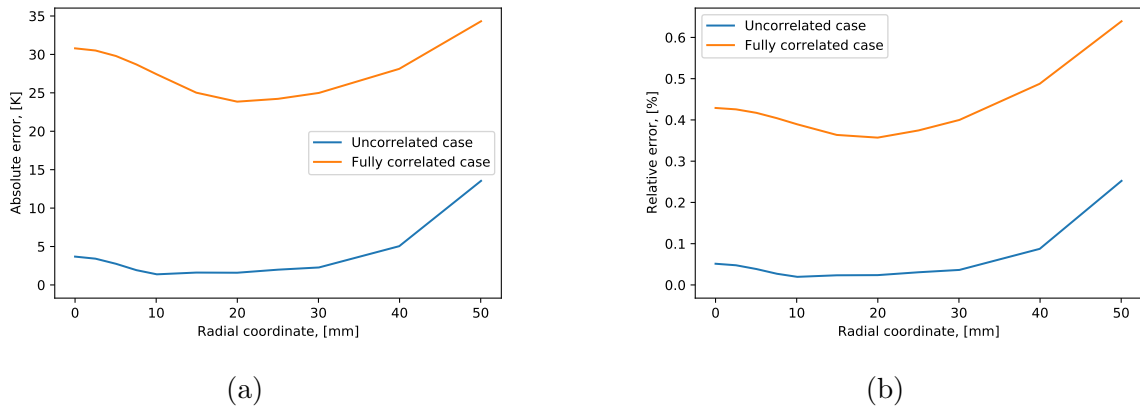
FIGURE 4.7: Error on the temperature measurement considering the uncertainty on the spectrum image.

4.1.3 Uncertainty on the background image

For a better accuracy on the results, a background image of the facility without the plasma is taken and then subtracted from the spectrum image of the plasma. An

example of a background image is given in Fig 4.8 as well as a histogram plot of all pixels in Fig 4.9.
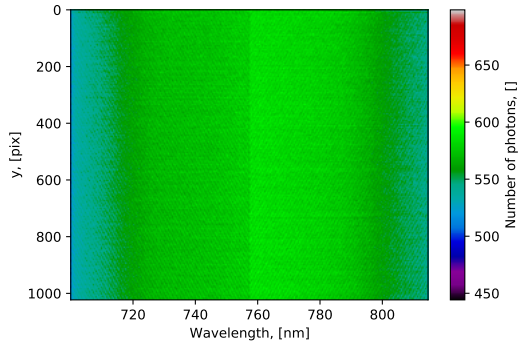

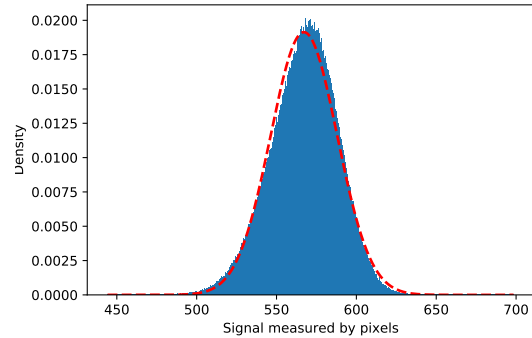FIGURE 4.8: Background image of the Plasmatron facility.

FIGURE 4.9: Histogram plot of the pixels constituting the background image.

The background is not perfectly uniform but the pixels are all included in a range of approximately 250 photons. That range is actually relatively small compared to the spectrum image which can go up to 25000 photons captured by pixel for regions of an emission line. Moreover, the shape of the histogram is nearly Gaussian which means that the probability distribution function of the background pixels can be approximated by a normal distribution (the red dotted line). This normal distribution has a mean value of 567.07 photon and a standard deviation of 23.1 photon.

Now, a random background can be generated by assuming that each pixel follows this normal distribution. The Monte Carlo method is used to propagate the uncertainties on the background image through the measurement chain. One thousand iterations are computed considering all other parameters constant. The one thousand temperatures at the center of the jet are plotted in Fig 4.10 and fitted by a normal distribution. This normal distribution has a standard deviation of 0.25 K meaning that 95% of the temperatures are contained in the interval 7177±0.5 K.

The one thousand temperatures at 50 mm from the center are plotted in Fig 4.10 and fitted by a normal distribution. This normal distribution has a standard deviation of 3.95 K meaning that 95% of the temperatures are contained in the interval 5367±7.9 K.
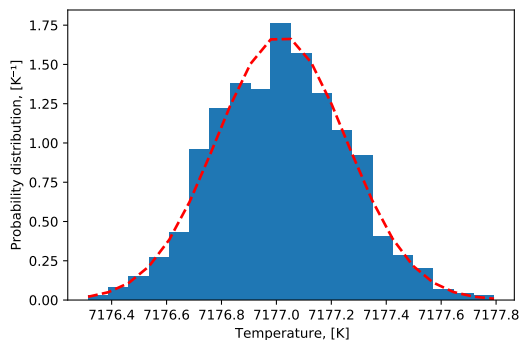

FIGURE 4.10: Temperature at the center of the jet considering the uncertainty on the background image.
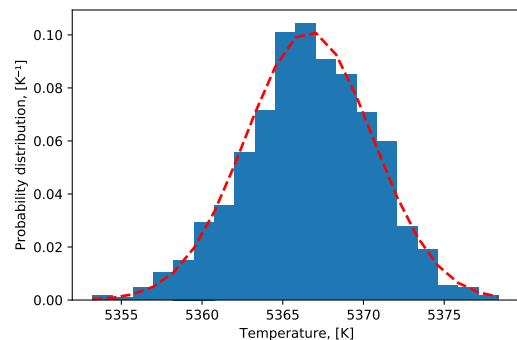

FIGURE 4.11: Temperature at 50 mm from the center considering the uncertainty on the background image.

The standard deviations of the background pixels are very small compared to the intensities in the spectrum image, explaining why this uncertainty has a minimal impact on the temperature. However, as the signal to noise ratio decreases, the uncertainty increases. For example, at the center of the jet, the signal to noise ratio is 44 and the uncertainties are ± 0.5 K. At 50 mm from the center, the signal to noise ratio drops to 2 and the uncertainties rise to ± 7.9 K.

The maximum error corresponding to two times the standard deviation is computed for each radial coordinate and plotted in Fig 4.12.
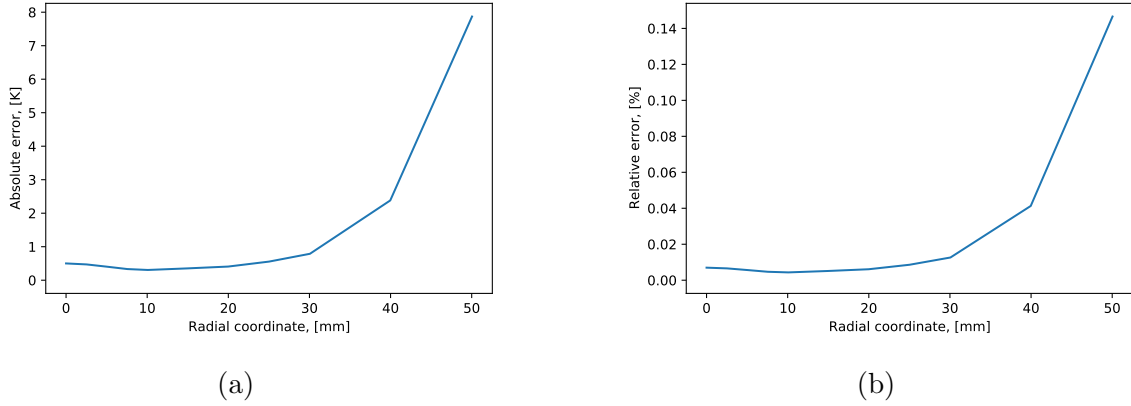
FIGURE 4.12: Error on the temperature measurement considering the uncertainty on the background image.

4.2 Calibration

A calibration is performed on each pixels in order to retrieve the value of the radiance using the following equation:

$$L_\lambda^{\mathrm{meas}} = \frac{S^{\mathrm{meas}}/\Delta t^{\mathrm{meas}}}{S^{\mathrm{calib}}/\Delta t^{\mathrm{calib}}} L_\lambda^{\mathrm{calib}} \tag{4.1}$$

Where $L_\lambda^{\mathrm{meas}}$ is the radiance of the plasma. $L_\lambda^{\mathrm{calib}}$ is the radiance of the calibration source which is known with an uncertainty. S^{meas} is the cleared signal measured by the camera when observing the plasma that is the spectrum image minus the background. This value has uncertainties as discussed in section 4.1.2. S^{calib} is the cleared signal measured by the camera when observing the calibration source that is also subjected to uncertainties. This signal is a spectrum image of the calibration source minus the background.

4.2.1 Uncertainty on the calibration image

The uncertainties on the calibration image are computed in the same way as for the plasma image. Ten spectrum images are taken, then an image is generated from the mean and the standard deviation of each pixel of the ten images considering a case with no correlations between the pixels and a case with full correlation between them.

The Monte Carlo method is used to propagate the uncertainties on the calibration image through the measurement chain. One thousand iterations are computed considering all other parameters constant.

The one thousand temperatures are plotted in Fig 4.5 for the uncorrelated case and fitted by a normal distribution. This normal distribution has a standard deviation of 0.85 K meaning that 95% of the temperatures are contained in the interval 7177±1.7 K.

Fig 4.6 plots the temperatures for the fully correlated case. The normal distribution has a standard deviation of 7.5 K meaning that 95% of the temperatures are contained in the interval 7177±15 K.
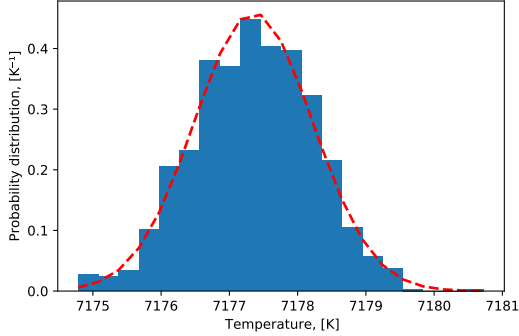

FIGURE 4.13: Temperature at the center of the jet considering the uncertainty on the calibration image for the uncorrelated case.
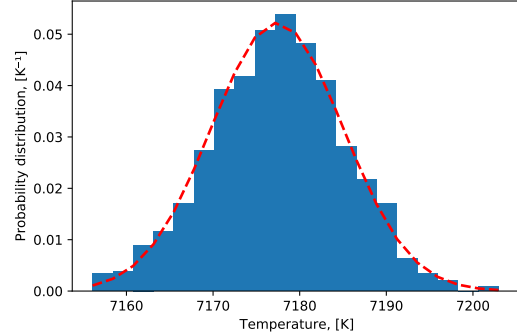
FIGURE 4.14: Temperature at the center of the jet considering the uncertainty on the calibration image for the fully correlated case.

The maximum error corresponding to two times the standard deviation is computed for each radial coordinate and plotted in Fig 4.15.
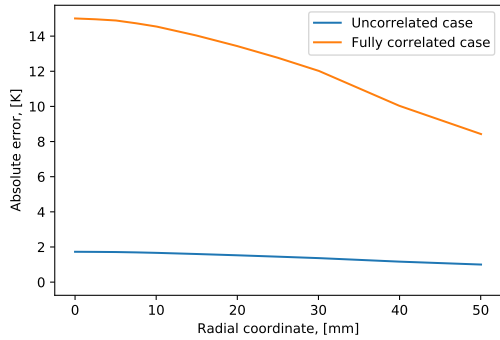
(a)
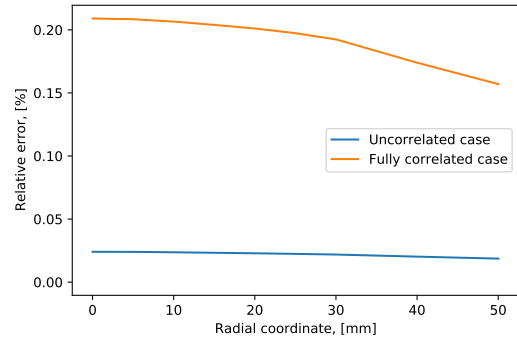
(b)

FIGURE 4.15: Error on the temperature measurement considering the uncertainty on the calibration image.

4.2.2 Uncertainty on the radiance of the calibration source

The radiance of the calibration source have been measured with uncertainties. However, this radiance depends on the wavelength. In the Monte Carlo method, a vector of radiance is randomly generated from the uncertainties. In the same way as or the spectrum image, the values of this vector might be correlated with each other. This correlation is unknown and impossible to determine with precision. In order to analyze the importance of this correlation, a case with completely uncorrelated values is considered as well as a case assuming fully correlated values.
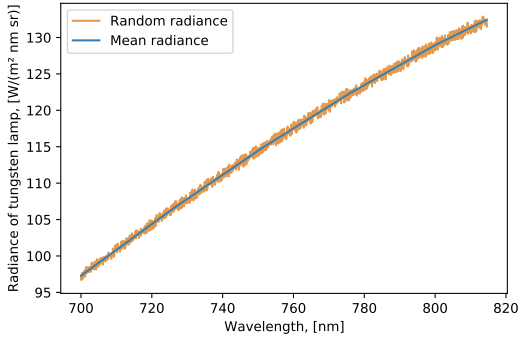
FIGURE 4.16: Radiance of calibration source generated considering uncorrelated random variables.
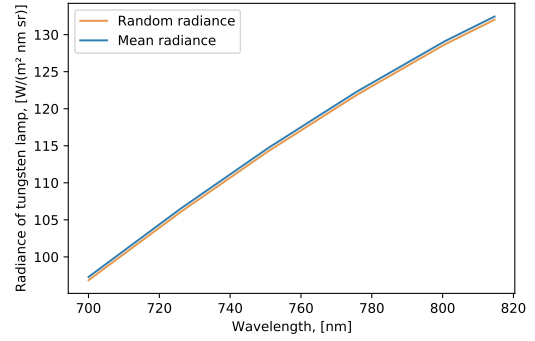

FIGURE 4.17: Radiance of calibration source generated considering fully correlated random variables.

The Monte Carlo method is used to propagate the uncertainties on the radiance of the calibration source through the measurement chain. One thousand iterations are computed considering all other parameters constant.

The one thousand temperatures are plotted in Fig 4.18 for the uncorrelated case and fitted by a normal distribution. This normal distribution has a standard deviation of 0.7 K meaning that 95% of the temperatures are contained in the interval 7177±1.3 K.

Fig 4.19 plots the temperatures for the fully correlated case. The normal distribution has a standard deviation of 1.35 K meaning that 95% of the temperatures are contained in the interval 7177±2.7 K.
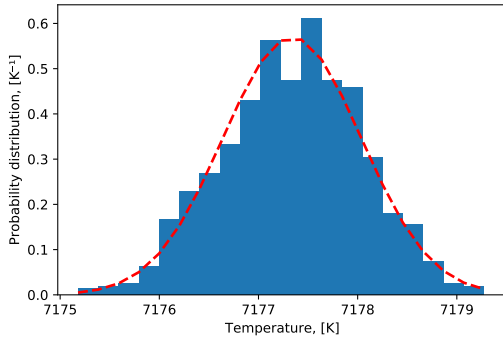

FIGURE 4.18: Temperature at the center of the jet considering the uncertainty on the radiance of the calibration source for the uncorrelated case.
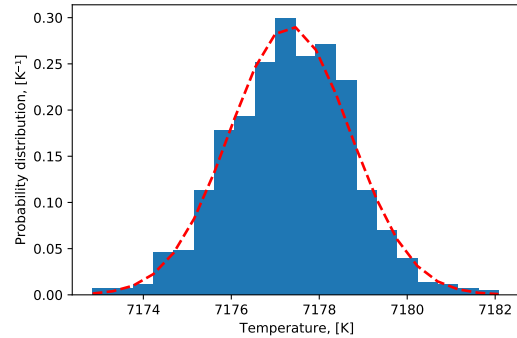

FIGURE 4.19: Temperature at the center of the jet considering the uncertainty on the radiance of the calibration source for the fully correlated case.

When the radiance is randomly generated considering uncorrelated values, it leads to smaller uncertainties in the final temperature. This is due to the fact that the uncertainties mostly cancel out after the integration of the emission line in the case of an uncorrelated vector.

The maximum error corresponding to two times the standard deviation is computed for each radial coordinate and plotted in Fig 4.20.
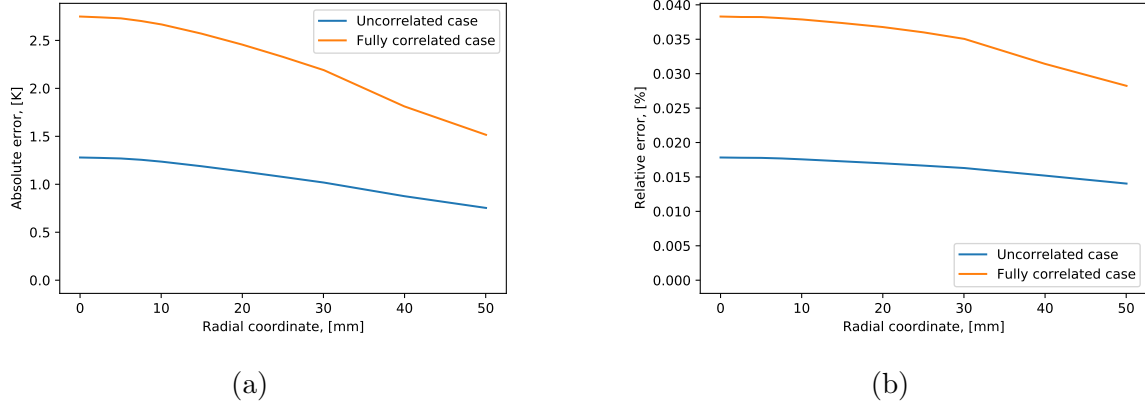
(a)	(b)

FIGURE 4.20: Error on the temperature measurement considering the uncertainty on the radiance of the calibration source.

4.3 Line selection and integration

4.3.1 Uncertainty on the baseline subtraction

At this state, only one portion of the calibrated image must be integrated in order to retrieve the line emission of an atom transition. However, the other atoms and molecules constituting the plasma radiate energy at different wavelength and the signal measured is actually a combination of all these radiations. At the considered wavelength, the radiation due to the atom transition is much stronger than all other radiations but these radiations should still be subtracted. The baseline is an approximation of the radiation from other atoms and molecules and is subtracted after the integration. The baseline is a line drawn between the two integration points. The boundaries of the integration must be far from the peak in order to account for all the energy of the peak but not too far to have an accurate approximation of the baseline.

In Fig 4.21 and Fig 4.22, an integration range is shown. The range is equal to six times the width at half maximum of the peak. If this range is smaller, the integration would not take into account all the energy of the peak. This range can also not be larger because in this case, the integration of the nitrogen line would be impacted by another emission line at 744.5 nm as it can be seen in Fig 4.22. This range of six times the width at half maximum is arbitrary so the effect of an alternative choice of integration range is studied below.
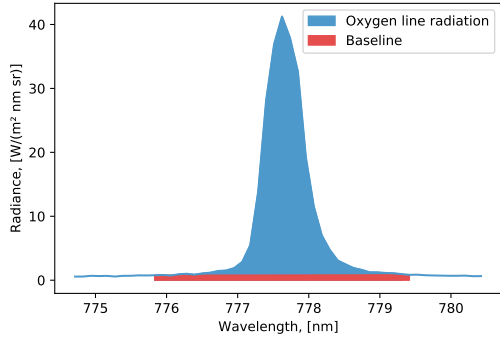
FIGURE 4.21: Emission of the central line centered at 777 nm showing the emission intensity of the oxygen triplet and the baseline emission.
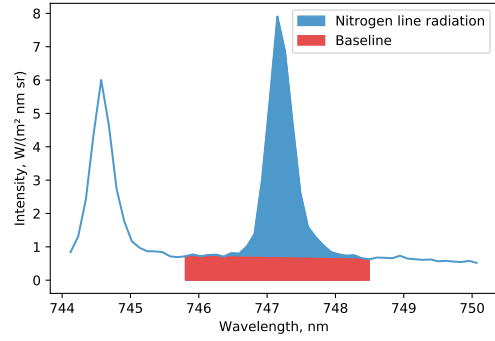

FIGURE 4.22: Emission of the central line centered at 747 nm showing the emission intensity of the nitrogen and the baseline emission.

Fig4.23 is a zoom in the left boundary of the integration of Fig 4.21 and shows that the radiation is very noisy. The baseline is drawn between the two integration points, so it depends only on these two values and changing these boundaries, even a little, could leads to a large variation on the baseline.
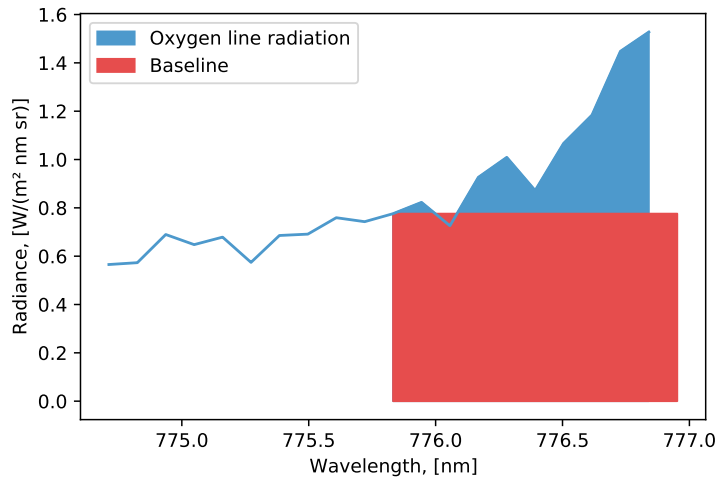

FIGURE 4.23: Zoom in Fig4.21 centered at the left boundary of the integration.

The dependency on the integration bounds can be reduced by averaging the noisy signal. Instead of taking only two points and drawing a line between them, five consecutive points are taken at the left boundary and five others at the right boundary. Then, a line is fitted through these ten points.

Now the baseline is more accurate but still has an uncertainty. This uncertainty is evaluated by considering an uncertainty on the boundary. Concretely, the boundaries are computed by taking six times the width at half maximum of the peak. Then, an uncertainty of ± 0.3 nm is applied to the boundaries. In this way, the baseline will vary at each iteration of the Monte Carlo method and account for the uncertainty coming from the approximation of the base radiation.

This uncertainty has a very small impact on the temperature computation because the signal to baseline ratio is very high. In Fig 4.24 and Fig 4.25, the signal to baseline ratio is plotted for the different radial coordinates for the oxygen triplet 777 nm and

the nitrogen line 747 nm respectively. It can be seen that the signal to baseline ratio is much lower for the nitrogen line 747 nm. Also, in both figure, at approximately 40 mm, the signal to baseline ratio increases while it should continue to decrease. This is due to the fact that both the signal and the baseline are very weak and are too affected by noise. The results after 40 mm, when the signal to baseline ratio starts to increase, are then considered irrelevant.
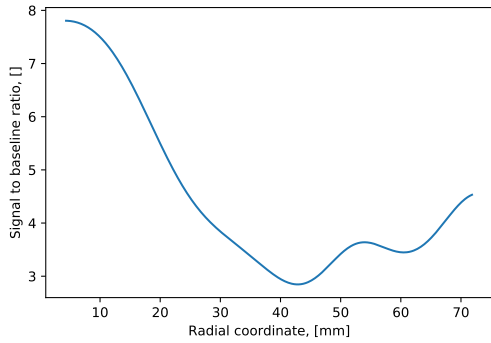

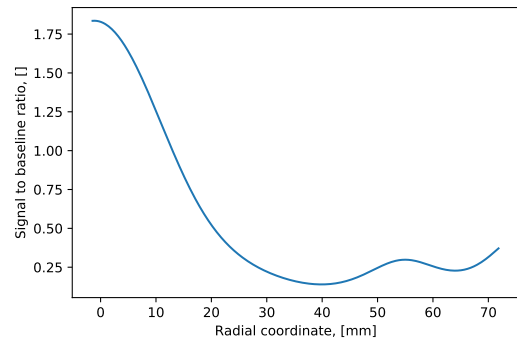FIGURE 4.24: Signal to baseline ratio of the emission of oxygen triplet 777 nm.

FIGURE 4.25: Signal to baseline ratio of the emission of nitrogen line 747 nm.

In Fig 4.26, the temperature is computed from the oxygen triplet 777 nm and from the nitrogen 747 nm. The Monte Carlo method is used to propagate the uncertainties on the baseline subtraction through the measurement chain. One thousand iterations are computed considering all other parameters constant. The figure shows that the uncertainties due to the baseline approximation are much larger for the nitrogen line where the signal to baseline ratio is smaller. It can also be seen that, after 40 mm, the temperatures diverge. As explained above, at this distance, the signal is too weak and the computation are too noisy which explains this divergence.
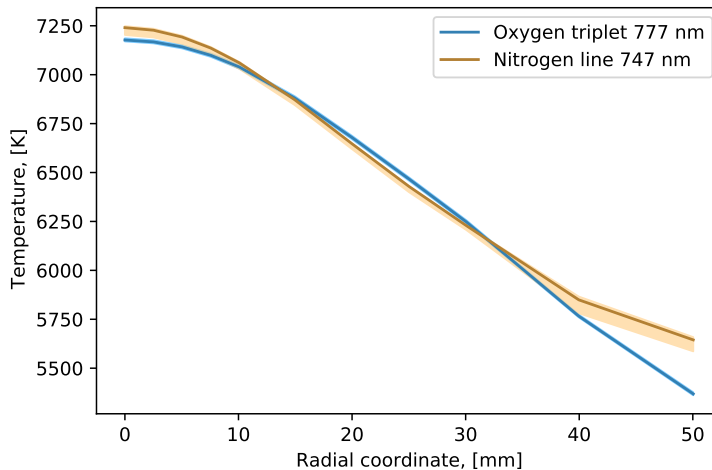

FIGURE 4.26: Uncertainties on the temperature accounting for the uncertainty on the baseline subtraction (the continue line is the nominal temperature).

The uncertainties on the temperature computed from the oxygen triplet 777 nm are 7177±7 K at the center of the jet and 5369±8 K at 50 mm from the center. For the uncertainties on the temperature computed from the nitrogen line 747 nm, they are 7235±15 K at the center of the jet and 5636±20 K at 50 mm from the center.

4.4 Abel inversion

4.4.1 Uncertainty on the spatial dimension

During the integration of an emission line, another calibration is performed. The spatial coordinate, which has a range of 1024 pixels, is converted to mm. This calibration is done by taking an image of a checkerboard pattern. Afterwards, by knowing the size of the pattern, the pixels are converted to a length in mm. Unfortunately, some pixels overlap two squares and counting the number of pixels in one square can be an arduous task as shown in Fig 4.27.
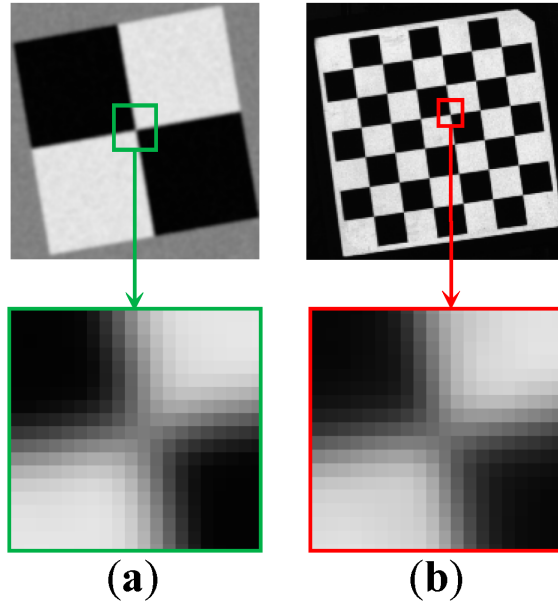

FIGURE 4.27: Example of a checkerboard pattern used for a spatial calibration.

The Abel inversion computes the local emission from the radiance but the equation involves the derivative of the radiance with respect to the spatial dimension. Therefore, an uncertainty on the spatial dimension will leads to an uncertainty on the local emission. In order to account for this uncertainty, a random variable is added to the number of pixels counted in one square. This variable has a uniform probability distribution between -0.5 and 0.5 pixel.

The Monte Carlo method is used to propagate the uncertainties on the spatial calibration through the measurement chain. One thousand iterations are computed considering all other parameters constant. The one thousand temperatures are plotted in Fig 4.28 and fitted by a normal distribution. This normal distribution has a standard deviation of 0.2 K meaning that 95% of the temperatures are contained in the interval 7177 ± 0.4 K.
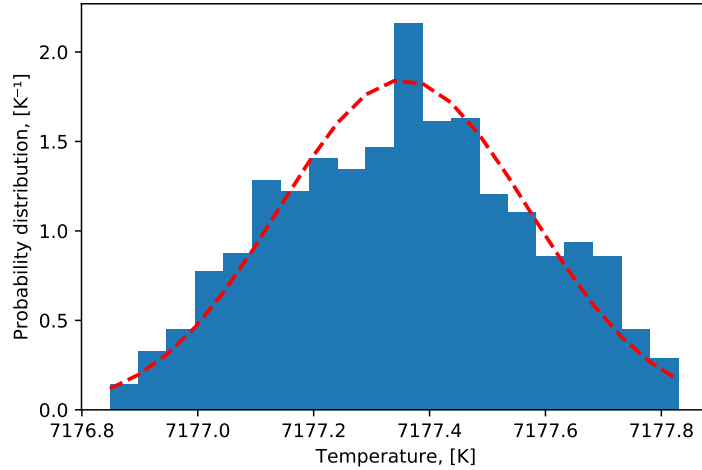
FIGURE 4.28: Temperature at the center of the jet considering the uncertainty on the spatial calibration.

The propagated uncertainty is very small because the uncertainty is only one pixel for the whole image which contains about one thousand pixels.

4.4.2 Uncertainty propagation

The Abel inversion computes the local emission from the radiance of the plasma. The uncertainties on the radiance computed above should therefore be propagated trough the Abel inversion. Thankfully, the Monte Carlo method allows a very simple propagation in this case. Indeed, in order to compute the uncertainties on the emission, the Abel inversion should simply be applied to the radiance without introducing uncertainties, as it is implemented in the measurement chain. The result of the propagation is plotted in Fig 4.29.
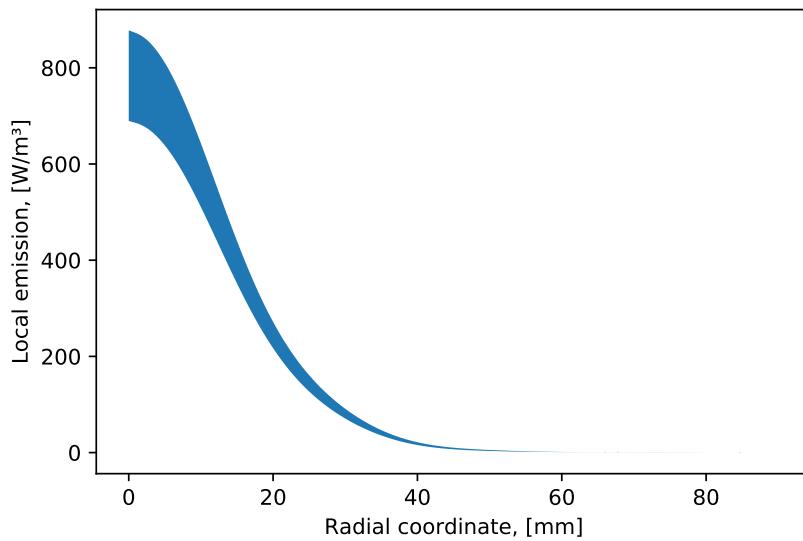

FIGURE 4.29: Uncertainty on the local emission of the jet considering the uncertainty on all parameters.

The results are now compared to an analytical method. However, there are several methods that can be used to compute an Abel inversion. In this thesis, the method used is the Hansen–Law [9] method and unfortunately, it is too complex and impossible to propagate by an analytical development. Therefore, another method is described in the next section and implemented for an analytical propagation.

4.4.3 Analytical propagation

Polynomial fitting

In this section, a polynomial fitting is used to compute the Abel inversion of the radiance. This method has the advantage of being simpler to implement than the method used previously. It is also possible to propagate the uncertainty by analytical development as done by Laux in his thesis [14]. A polynomial fitting is used to smooth the curve of radiance and also allows the equation of the Abel inversion to be very simple to apply. With $L_\lambda = a_0 + a_1 x + a_2 x^2 + \ldots + a_m x^m$, equation 2.3 becomes:

$$\epsilon_\lambda(r) = \frac{1}{\pi} \left[\int_r^R \frac{a_1}{\sqrt{x^2 - r^2}} dx + \int_r^R \frac{2a_2 x}{\sqrt{x^2 - r^2}} dx + \ldots + \int_r^R \frac{m a_m x^{m-1}}{\sqrt{x^2 - r^2}} dx \right] \quad (4.2)$$

The degree of the polynomial is chosen large enough to fit the data well but not too large to limit the time of computation. The radiance is radially symmetric and then has a zero slope at the center line. The coefficient a_1 is set to zero to satisfy this condition. Here are some examples of fitting:
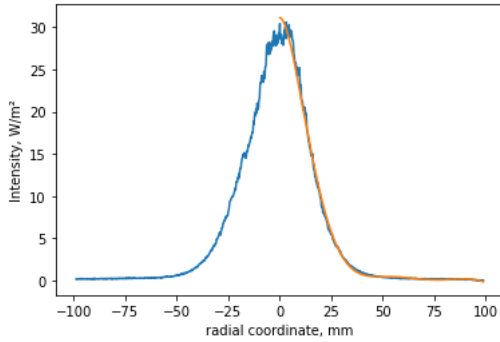

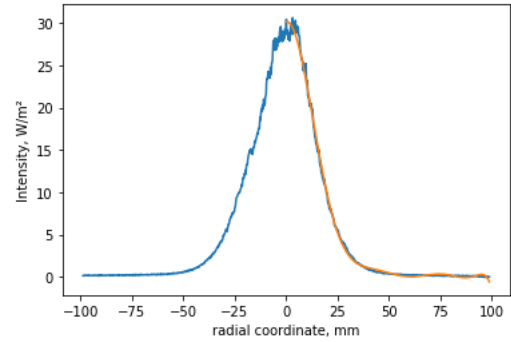FIGURE 4.30: Fitting of the radiance by a polynomial of degree 7.

FIGURE 4.31: Fitting of the radiance by a polynomial of degree 9.
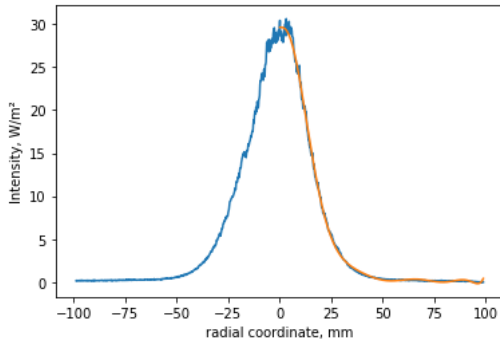

FIGURE 4.32: Fitting of the radiance by a polynomial of degree 10.
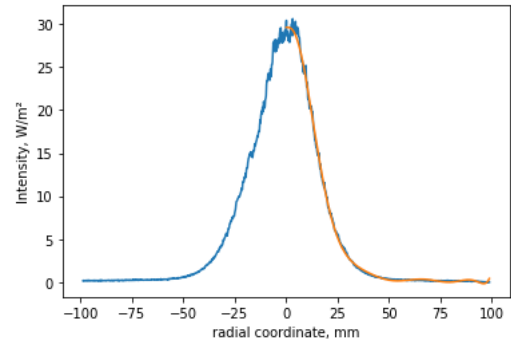

FIGURE 4.33: Fitting of the radiance by a polynomial of degree 20.

Particular attention should be paid to the center line because the result of the Abel inversion is greatly dependent on this value. No difference can be seen between a polynomial of degree 10 and a polynomial of degree 20 while degree 9 differs slightly. These polynomials are Abel inverted to retrieve the local emission:
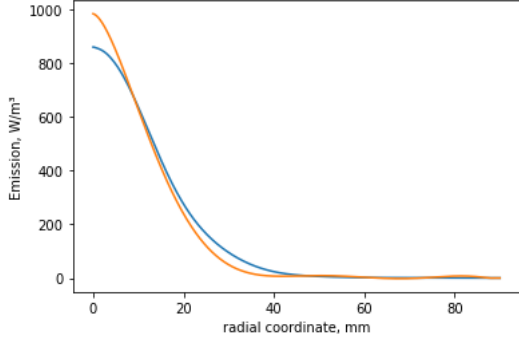

FIGURE 4.34: Abel inversion of a polynomial of degree 8 (in orange) in comparison with an other method (in blue).
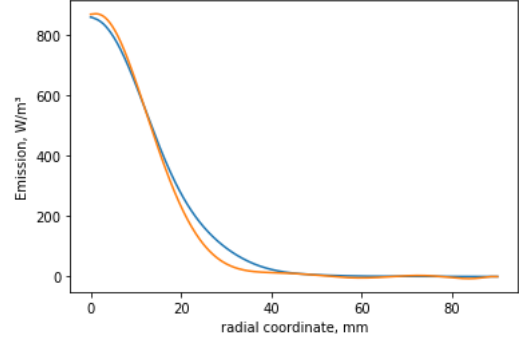

FIGURE 4.35: Abel inversion of a polynomial of degree 9 (in orange) in comparison with an other method (in blue).
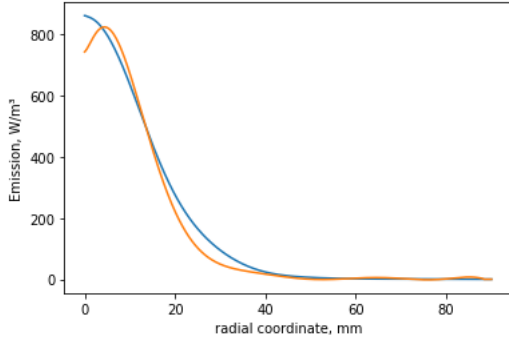

FIGURE 4.36: Abel inversion of a polynomial of degree 10 (in orange) in comparison with an other method (in blue).
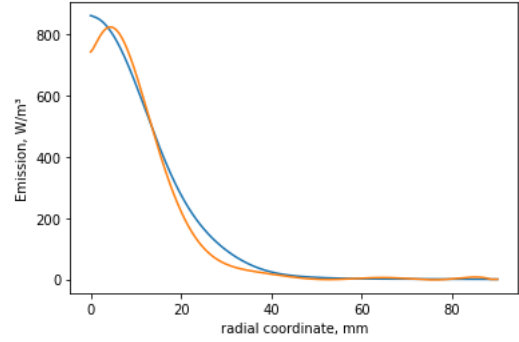

FIGURE 4.37: Abel inversion of a polynomial of degree 11 (in orange) in comparison with an other method (in blue).

The results are compared to the Hansen–Law method which uses Fourier transforms. After degree 10, the degree is too high and the polynomial starts to fit the variation due to the noise. This increasing slope at the central line is an error of the fitting and does not exist in reality. The polynomial of degree 9 gives the closest result to the first method which is supposed to be the best. This polynomial is therefore used for the next computations.

Propagation of uncertainty

For a set of data $X = (x_1, x_2, ..., x_n)^T$ where x_i is a realization of a random variable, the covraiance matrix is defined as:

$$\Sigma_X = \overline{(X - \overline{X})(X - \overline{X})^T} \tag{4.3}$$

Where $\overline{X}$ is the mean of all the realizations of the random variable. A linear transform can be applied to this set of data to give:

$$Y = AX + B \tag{4.4}$$

Now computing the covariance of the new set of data leads to:

$$\begin{aligned}
\Sigma_Y &= \overline{(AX + B - \overline{AX + B})(AX + B - \overline{AX + B})^T} \\
&= \overline{(AX + B - (A\overline{X} + B))(AX + B - (A\overline{X} + B))^T} \\
&= \overline{(AX - A\overline{X})(AX - A\overline{X})^T} \\
&= A\overline{(X - \overline{X})(X - \overline{X})^T}A^T \\
&= A\Sigma_X A^T
\end{aligned}$$

(4.5)

Both the polynomial fitting and the Abel inversion are linear transform. Therefore, the covariance matrix can simply be propagated using Equation 4.5.

The polynomial fitted is the function: $I = a_0 + a_2 x^2 + ... + a_m x^m$ so that a set of points $\boldsymbol{D} = (I_1/\sigma_{d_1}, \ldots, I_n/\sigma_{d_n})$ is a linear function of the fitting coefficients and of a constant vector:

$$\boldsymbol{D} = \boldsymbol{P}\boldsymbol{R_F} + \boldsymbol{C} = \begin{pmatrix} \frac{x_1^2}{\sigma_{d_1}} & \frac{x_1^3}{\sigma_{d_1}} & \cdots & \frac{x_1^m}{\sigma_{d_1}} \\ \vdots & & & \vdots \\ \vdots & & & \vdots \\ \vdots & & & \vdots \\ \frac{x_n^2}{\sigma_{d_n}} & \frac{x_n^3}{\sigma_{d_n}} & \cdots & \frac{x_n^m}{\sigma_{d_n}} \end{pmatrix} \begin{pmatrix} a_2 \\ a_3 \\ \vdots \\ a_m \end{pmatrix} + \begin{pmatrix} \frac{a_0}{\sigma_{d_1}} \\ \vdots \\ \vdots \\ \vdots \\ \frac{a_0}{\sigma_{d_n}} \end{pmatrix}$$

(4.6)

In Eq 4.6, $\mathbf{D}$ is known and the vector of the fitting coefficient is the unknown. The equation should then be rewritten. After some transformations, the vector of coefficient is expressed as a function of the radiance:

$$\begin{aligned}
\mathbf{P}^T\mathbf{D} &= \mathbf{P}^T\mathbf{P}\mathbf{R_F} + \mathbf{P}^T\mathbf{C} \\
(\mathbf{P}^T\mathbf{P})^{-1}\mathbf{P}^T\mathbf{D} &= \mathbf{R_F} + (\mathbf{P}^T\mathbf{P})^{-1}\mathbf{P}^T\mathbf{C} \\
\mathbf{R_F} &= (\mathbf{P}^T\mathbf{P})^{-1}\mathbf{P}^T\mathbf{D} - (\mathbf{P}^T\mathbf{P})^{-1}\mathbf{P}^T\mathbf{C}
\end{aligned}$$

(4.7)

Which is a linear transformation with $A = (\mathbf{P}^T\mathbf{P})^{-1}\mathbf{P}^T\mathbf{D}$ and $B = -(\mathbf{P}^T\mathbf{P})^{-1}\mathbf{P}^T\mathbf{C}$. The covariance matrix of the fitting coefficient is then: $\Sigma_{\mathbf{R_F}} = A\Sigma_{\mathrm{D}}A^T$. Where Σ_{D} is the covariance matrix of the radiance.

Since the Abel inversion is also a linear transformation, it is again possible to propagate the uncertainty using the formula: $\Sigma_{\mathbf{R}} = A\Sigma_{\mathbf{R_F}}A^T$. The Abel inversion equation can be written:

$$\mathbf{R} = A\mathbf{R_F} = -\frac{1}{\pi} \begin{pmatrix} \int_{r_1}^{R} \frac{2x\,dx}{\sqrt{x^2-r_1^2}} & \cdots & \int_{r_1}^{R} \frac{mx^{m-1}\,dx}{\sqrt{x^2-r_1^2}} \\ \vdots & & \vdots \\ \int_{r_n}^{R} \frac{2x\,dx}{\sqrt{x^2-r_n^2}} & \cdots & \int_{r_n}^{R} \frac{mx^{m-1}\,dx}{\sqrt{x^2-r_n^2}} \end{pmatrix} \begin{pmatrix} a_2 \\ a_3 \\ \vdots \\ a_m \end{pmatrix}$$

(4.8)

Now that this covariance matrix of the local emission is computed, it can be compared to the uncertainty computed by the Monte Carlo method. For a more visual comparison, 1000 samples computed with the Monte Carlo method are plotted in Fig 4.38 next to Fig 4.39 which shows 1000 curves randomly generated from the covariance matrix calculated with the analytical method.
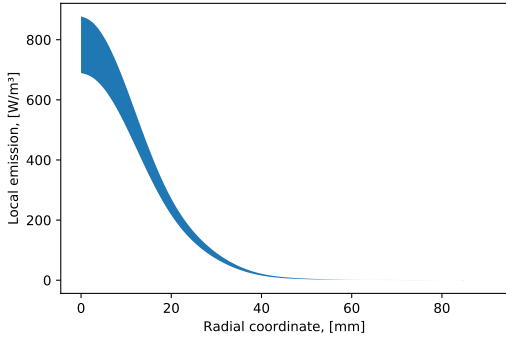
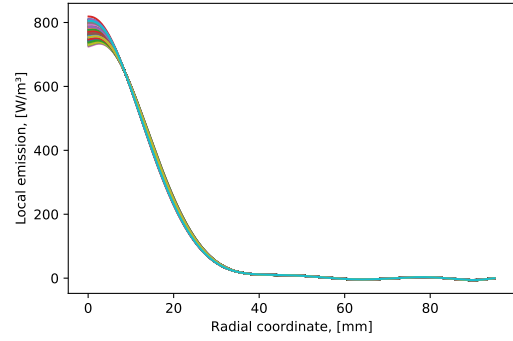FIGURE 4.38: Emission computed after the abel inversion.

FIGURE 4.39: Emission generated using the covariance matrix propagated.

These two graphs show the same results and therefore validate the two methods. However, they also show the limitation of the analytical method. For example, around 10 mm, a node appears but is obviously not representative of the reality. Moreover, the polynomial is bad at fitting the extremity and this fact can be seen after 40 mm where the emission has some oscillations that are only due to the fitting and do not exist in reality.

4.5 Temperature computation

4.5.1 Uncertainty on the Einstein coefficient

The equation 4.9 used to compute the population of atoms in the exited state involves the Einstein Coefficient A_u which has been measured and registered in the NIST database with an uncertainty of 3% [11].

$$\epsilon_{\mathrm{ul}} = \frac{E_{\mathrm{u}} - E_1}{4\pi} \mathcal{A}_{\mathrm{ul}} n_{\mathrm{u},i} \tag{4.9}$$

Unfortunately, the database does not provide any information about what this 3% actually means. It could be a strict bound where the probability is constant within the interval or the probability distribution function could be a normal distribution which is more representative of the reality. In this case, the 3% would be equal to two times the standard deviation meaning that the real Einstein coefficient has a probability of 95% of being included in the interval $\pm 3\%$.

The two cases are considered with first, on Fig 4.40, the uncertainty propagated considering that the Einstein coefficient has a constant probability distribution function and on Fig 4.41, the uncertainty propagated considering a normal distribution.
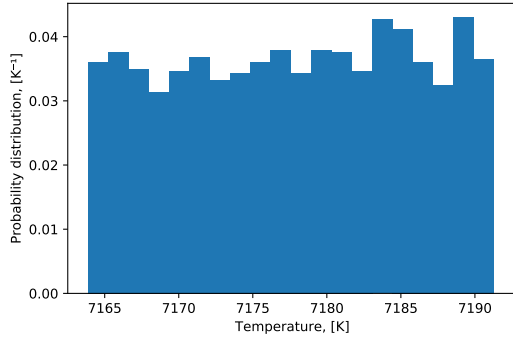
FIGURE 4.40: Temperature at the center of the jet considering the uncertainty on the Einstein coefficient and a constant distribution.
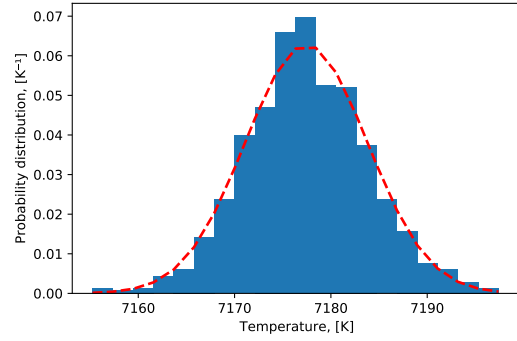

FIGURE 4.41: Temperature at the center of the jet considering the uncertainty on the Einstein coefficient and a normal distribution.

The probability function is nearly constant in Fig 4.40 because the Einstein coefficient varies very little which leads to a propagation through the measurement chain that is almost linear. Since the uncertainty is computed from a uniform distribution, the propagated uncertainty is also uniform.

The uncertainty on the temperature is 7177±16 K considering strict bounds and a constant probability distribution on the input and 7177±13.9 K considering a normal distribution.

The maximum error corresponding to two times the standard deviation is computed for each radial coordinate and plotted in Fig 4.42.
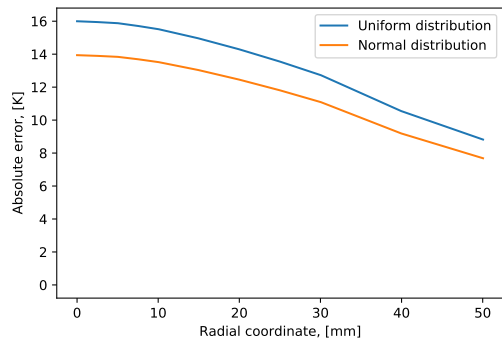
(a)
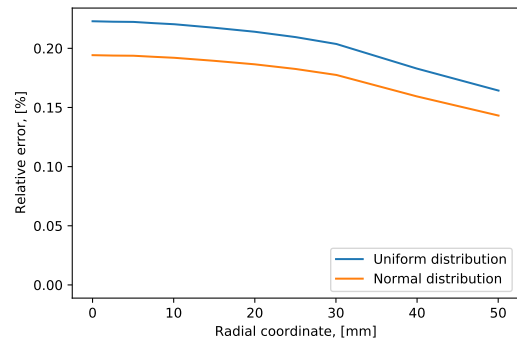
(b)

FIGURE 4.42: Error on the temperature measurement considering the uncertainty on the Einstein coefficient.

4.5.2 Uncertainty on the pressure

The plasma is assumed to be in local thermodynamic equilibrium, therefore, the population of atoms in the exited level follows a Boltzmann distribution computed with:

$$n_{\mathrm{u},i} = n_i \left(T_{\mathrm{LTE}}, p \right) \frac{g_{\mathrm{u},i} \exp\left(-\frac{E_{\mathrm{u},i}}{k_{\mathrm{B}} T_{\mathrm{LTE}}} \right)}{Q_{\mathrm{int},i} \left(T_{\mathrm{LTE}} \right)} \tag{4.10}$$

In this equation, $Q_{\mathrm{int},i}$ is a function of the temperature and can be considered without uncertainty. The ground population is a function of the temperature and the pressure

40

and is also considered without uncertainty. Here the pressure inside the chamber is measured with an uncertainty of 2%.

Like the Einstein coefficient, this uncertainty can be understood in two ways. In Fig 4.43, the probabilities are propagated considering that the probability distribution function of the pressure is constant. If it is considered that the probability distribution function is normal and that the 2% corresponds to two times the standard deviation, the propagated uncertainty leads to the temperatures depicted in Fig 4.44.
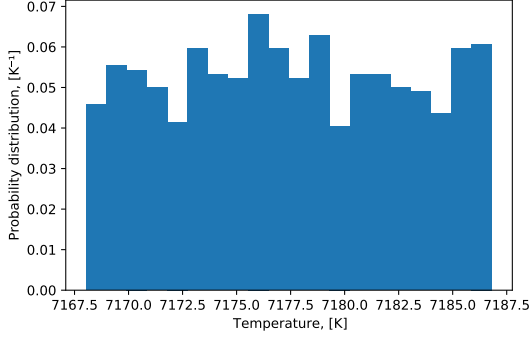

FIGURE 4.43: Temperature at the center of the jet considering the uncertainty on the pressure and a constant distribution.
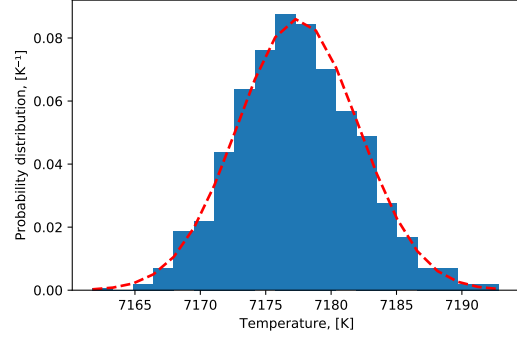
FIGURE 4.44: Temperature at the center of the jet considering the uncertainty on the pressure and a normal distribution.

In fig 4.43, the pressure has a constant probability distribution function because the propagation is almost linear. The uncertainty in this case is 7177±10.7 K and 7177±9.8 K when a normal distribution is considered.

The maximum error corresponding to two times the standard deviation is computed for each radial coordinate and plotted in Fig 4.45.
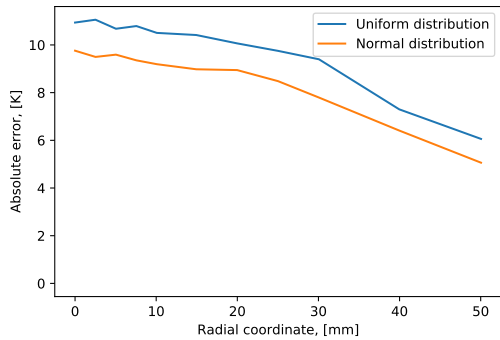
(a)
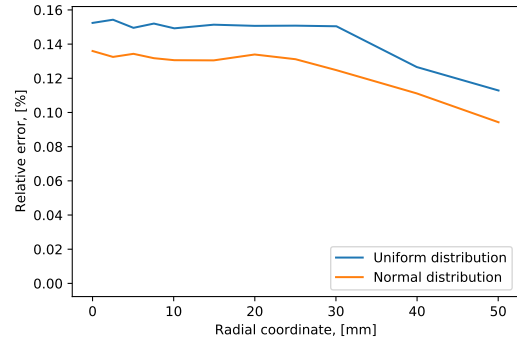
(b)

FIGURE 4.45: Error on the temperature measurement considering the uncertainty on the pressure.

4.6 Complete problem and final results

4.6.1 Uncertainties on all parameters combined

The temperature can be computed from different emission lines. In Fig 4.46 two temperature computations using the oxygen and the nitrogen lines are compared with

the uncertainties on these computations. The uncertainties are propagated using the Monte Carlo method with ten thousand iterations. More iterations are needed in order to have an accurate uncertainty propagation because in this case, all eight uncertain parameters are considered.

Some parameters could be generated in different ways. For example, the spectrum image and the calibration image have been generated by considering different cases of correlation between the pixels. For this computation, only the cases that lead to the largest uncertainties are considered. In this way, the computed uncertainties will be larger than the actual uncertainties, which ensures that the real temperature will be included in the computed interval.
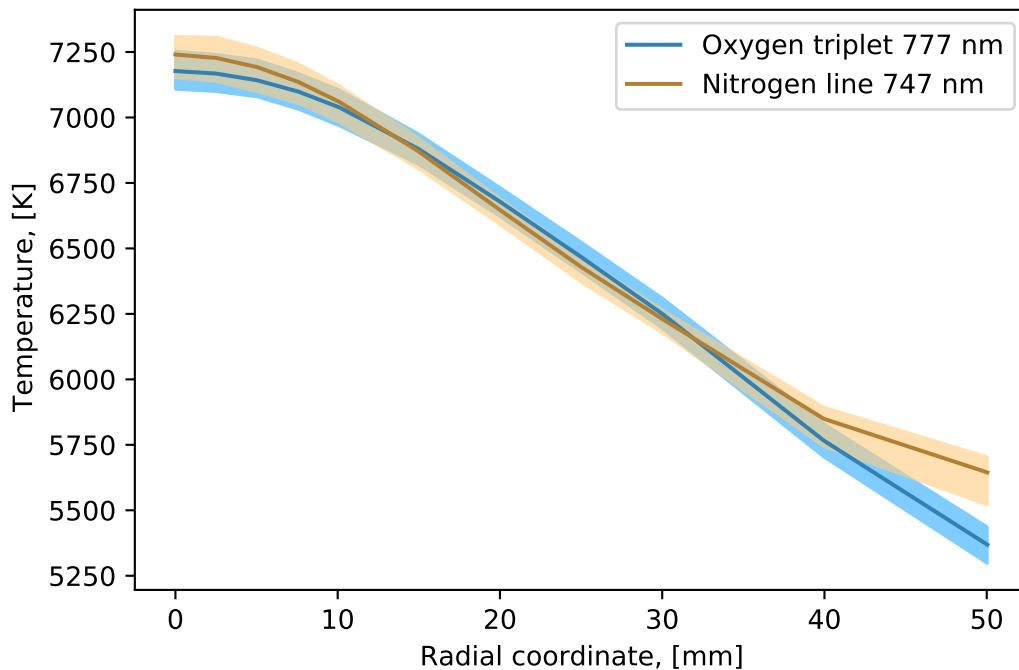
FIGURE 4.46: Uncertainties on the temperature accounting for the uncertainty on all parameters (the continue line is the nominal temperature).

The temperatures computed from the nitrogen line at 747 nm diverge after 40 mm from the center of the jet. This divergence can also be observed in the validation in section 2.6. In the same section, it was concluded that this divergence was due to the baseline subtraction which is a bad approximation especially for low signal to baseline ratios.

Concerning the temperatures computed from the oxygen triplet, the propagated uncertainties at the center of the jet are plotted in Fig 4.47 next to the temperature at 50 mm from the center at Fig4.48

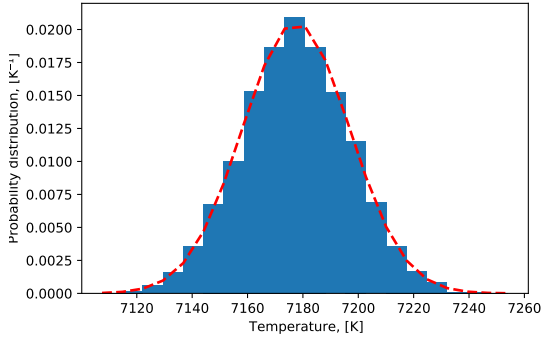FIGURE 4.47: Temperature at the center of the jet considering the uncertainties on all parameters
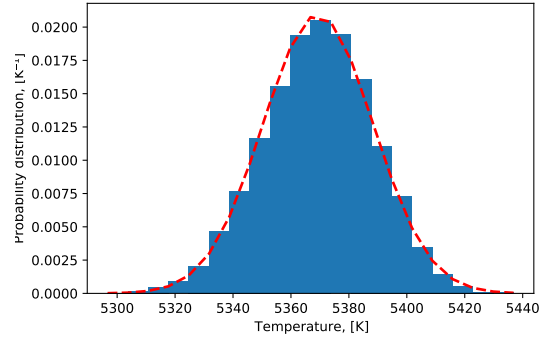
FIGURE 4.48: Temperature at 50 mm from the center considering the uncertainties on all parameters

At the center, 95% of the temperatures are included in the interval 7177±38.9 K while at 50 mm, this interval is 5369±38.1 K. In terms of percentages, that is an uncertainty of 0.54 % at the center and 0.71% at 50 mm.

Concerning the temperatures computed from the nitrogen line 747 nm, the propagated uncertainties at the center of the jet are 7235±40 K and 5636±44.6 at 50 mm from the center. In terms of percentages, that is an uncertainty of 0.55 % at the center and 0.79% at 50 mm.

The maximum error corresponding to two times the standard deviation is computed for each radial coordinate and plotted in Fig 4.49.
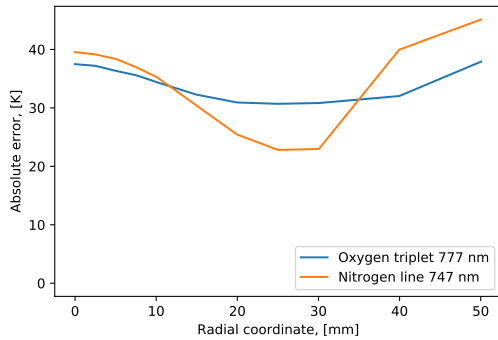
(a)
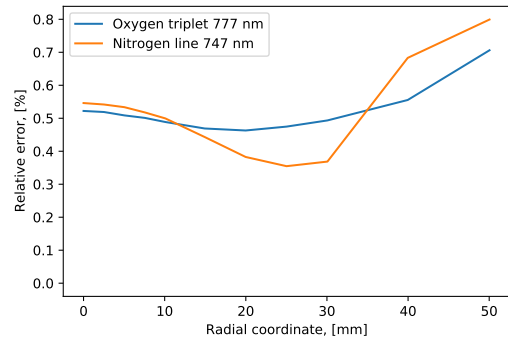
(b)

FIGURE 4.49: Error on the temperature measurement considering the uncertainty on all parameters.

4.6.2 Summary

Each parameter has a different impact on the temperature. To remind, all parameters considered and their impact on the central temperature are the following:

- Uncertainty on the plasma spectrum image, $\pm$ 30.5 K for the fully correlated case

- Uncertainty on the calibration spectrum image, $\pm$ 15 K for the fully correlated case

- Uncertainty on the Einstein coefficient, $\pm$ 13.9 K

- Uncertainty on the pressure, $\pm$ 9.8 K

- Uncertainty on the radiance of calibration source, $\pm$ 2.7 K for the fully correlated case

- Uncertainty on the baseline subtraction, $\pm$ 0.7 K

- Uncertainty on the background image, $\pm$ 0.5 K

- Uncertainty on the spatial calibration, $\pm$ 0.4 K

The sum of all these uncertainties is 73.5 which is larger than the uncertainty computed by considering all the uncertainties. Actually, these uncertainties correspond to two times the standard deviation and the combined uncertainty is not computed by the sum of the uncertainties but by:

$$\sigma_{tot} = \sqrt{\sum_{i=1}^{n} \sigma_i^2} \tag{4.11}$$

Applying this equation leads to a total standard deviation of $\sigma_{tot} = 19.06\ K$ or an uncertainty of ± 38.1 K. This result is much closer to the computed uncertainty which is ± 38.9 K. In this equation, the standard deviations are squared implying that the larger uncertainties have a larger impact on the temperature than smaller ones. This means that accounting for more small uncertainties would have a very small effect on the temperature computation.

Chapter 5

Conclusion

A data processing procedure was implemented to measure the temperature of the plasma jet from locally resolved emission spectroscopy measurements. The procedure focused on the atomic emission of the oxygen and nitrogen lines. The code was validated using a spectrum generated with SPECAIR. The procedure was analyzed at each step to identify possible sources of uncertainty in the measured quantity. Eight parameters were investigated: the measurement spectra, the calibration spectra, the Einstein coefficient, the pressure, the radiance of the calibration source, the baseline subtraction, the background image and the spatial calibration.

These uncertainties were propagated through the measurement chain using the Monte Carlo method in order to computed the total uncertainty on the temperature. The propagated uncertainty depends on the emission line used to retrieve the temperature. If a strong line is used, like the oxygen triplet at 777 nm, the uncertainty is about ±35 K for all radial coordinates of the jet. If the temperature is computed from a weaker line however, the uncertainty is close to ±40 K at the center of the jet but increases to ±45 at 50 mm from the center.

These results can be compared to the uncertainty propagation performed by Laux [14] on another plasma facility in 1993. In his study, Laux considered the uncertainty on the measured spectrum, the calibration and the Einstein coefficient and computed a total uncertainty of about 100 K. This difference can be explain by the fact that the uncertainties on the parameters were larger at that time. For example, in his report, the Einstein coefficient is given with an uncertainty of 10% while the uncertainty propagated in this thesis is only 3%.

Among these eight parameters, some uncertainties could not be accurately determined. In the spectrum images, the correlation between pixels is still unknown but two different cases were still considered in this thesis. Investigating the correlation between pixels would lead to a better estimation of the uncertainties on the temperature. The vector of the radiances of the calibration source also has an unknown correlation but once more, two correlation cases were implemented. The probability distribution function of the Einstein coefficient and the pressure is also unknown but a constant distribution and a normal distribution were both implemented and found to have a very small impact on the final uncertainty.

Some parameters still have uncertainties that were not investigated in this thesis. The unsteadiness of the plasma have been discussed but the uncertainties could not be estimated. Another uncertainty can come from the assumption of local thermodynamic equilibrium. It has been assumed that the plasma is in local thermodynamic equilibrium, but even if this approximation is very close to reality, it involves uncertainties.

The asymmetry of the plasma is also an uncertainty that was not implemented. Due to buoyancy, the plasma at the top is a little hotter than the plasma at the bottom. This problem was solved by taking the average of the top and bottom but this of course generates uncertainties.

Finally, taking into account smaller uncertainties would not have a meaningful impact on the total uncertainty since it is equal to the root sum of the squared individual uncertainties. This thesis focused on the most significant uncertain parameters. Therefore, it is a good estimation of the uncertainty on the temperature and allow a better understanding on the measurement steps that should be improved in order to increase the accuracy of the temperature computation.

Bibliography

[1] M. Arnst and J.-P. Ponthot. An overview of nonintrusive characterization, propagation, and sensitivity analysis of uncertainties in computational mechanics. *International Journal for Uncertainty Quantification*, 4(5):387–421, 2014.

[2] S. Caristia, F. De Filippis, A. Vecchio, and E. Graps. Scirocco pwt facility for high temperature material assembly testing. 09 2003.

[3] G. Castro, M. Mazzaglia, D. Nicolosi, and D. Mascali. Application of optical emission spectroscopy to high current proton sources. *Journal of Physics Conference Series*, 874, June 2017. `doi:10.1088/1742-6596/874/1/012033`.

[4] A. Cipullo, B. Helber, F. Panerai, L. Zeni, and O. Chazot. Investigation of freestream plasma flow produced by inductively coupled plasma wind tunnel. *Journal of Thermophysics and Heat Transfer*, 28(3), July 2014. `doi:10.2514/1.T4199`.

[5] J. Coheur. Sensitivity analysis and uncertainty quantification of plasma jet instabilities in the vki plasmatron, 2015.

[6] M. G. Cox and B. R. L. Siebert. The use of a monte carlo method for evaluating uncertainty and expanded uncertainty. *Metrologia*, 43(4):S178–S188, August 2006. `doi:10.1088/0026-1394/43/4/s03`.

[7] A. Fagnani, D. Le Quang Huy, B. Helber, S. Demange, A. Turchi, O. Chazot, and A. Hubin. Investigation of a free-stream air plasma flow by optical emission spectroscopy and comparison to magnetohydrodynamics simulations. In *AIAA Scitech 2020 Forum*, Orlando, FL, January 2020. American Institute of Aeronautics and Astronautics. `doi:https://doi.org/10.2514/6.2020-0382`.

[8] K. Fujita, M. Mizuno, K. Ishida, and T. Ito. Spectroscopic flow evaluation in inductively coupled plasma wind tunnel. *Journal of Thermophysics and Heat Transfer*, 22(4):685–694, 2008. `doi:10.2514/1.34032`.

[9] E. W. Hansen and P.-L. Law. Recursive methods for computing the abel transform and its inverse. *J. Opt. Soc. Am. A*, 2(4):510–520, Apr 1985. `doi:10.1364/JOSAA.2.000510`.

[10] D. L. Q. Huy. *Spectroscopic measurements of sub- and supersonic plasma flows for the investigation of atmospheric re-entry shock layer radiation*. PhD thesis, Université Blaise Pascal & von Karman Institute for Fluid Dynamics, June 2014.

[11] A. Kramida, Y. Ralchenko, and J. Reader. Nist atomic spectra database. 2020. `doi:https://dx.doi.org/10.18434/T4W30F`.

[12] H.-J. Kunze. *Introduction to Plasma Spectroscopy.* Springer Series on atomic, optical, and plasma physics, july 2009. `doi:10.1007/978-3-642-02233-3`.

[13] C. Laux. Radiation and nonequilibrium collisional-radiative models. *Von Karman Institute Lecture Series Physico-Chemical Modeling of High Enthalpy and Plasma Flows*, pages 2002–2007, January 2000.

[14] C. O. Laux. *Optical diagnostics and radiative emission of air plasmas.* PhD thesis, Department of machanical engineering of Stanford university, 1993.

[15] F. Panerai. *Aerothermochemistry Characterization of Thermal Protection Systems.* PhD thesis, von Karman Institute for Fluid Dynamics & Universitá degli Studi di Perugia, 2012.

[16] M. Playez. *Titan atmosphere plasma characterization using spectroscopic measurement techniques.* PhD thesis, Ecole Centrale Paris & von Karman Institute for Fluid Dynamic, June 2006.

[17] J. R. Roberts. Optical emission spectroscopy on the gaseous electronics conference rf reference cell. *Journal of research of the National Institute of Standards and Technology*, 100(4), January 1996. `doi:10.6028/jres.100.027`.

[18] J. B. Scoggins, V. Leroy, G. Bellas-Chatzigeorgis, B. Dias, and T. E. Magin. Mutation++: Multicomponent thermodynamic and transport properties for ionized gases in c++. *SoftwareX*, 12, December 2020. `doi:10.1016/j.softx.2020.100575`.

[19] R. C. Smith. *Uncertainty Quantification.* SIAM, Computational Science and Engineering Series, 2014.